On the constraints on superconducting cosmic strings from 21-cm cosmology

T. Gessey-Jones [1,2]★ S. Pochinda [1,2] H. T. J. Bevins [1,2] A. Fialkov,[2,3] W. J. Handley [1,2]
E. de Lera Acedo,[1,2] S. Singh[4] and R. Barkana [5]

[1]*Astrophysics Group, Cavendish Laboratory, J. J. Thomson Avenue, Cambridge, CB3 0HE, UK*
[2]*Kavli Institute for Cosmology, Madingley Road, Cambridge CB3 0HA, UK*
[3]*Institute of Astronomy, University of Cambridge, Madingley Road, Cambridge, CB3 0HA, UK*
[4]*Raman Research Institute, C V Raman Avenue, Sadashivanagar, Bangalore 560080, India*
[5]*School of Physics and Astronomy, Tel-Aviv University, Tel-Aviv 69978, Israel*

ABSTRACT

Constraints on the potential properties of superconducting cosmic strings provide an indirect probe of physics beyond the standard model at energies inaccessible to terrestrial particle colliders. In this study, we perform the first joint Bayesian analysis to extract constraints on superconducting cosmic strings from current 21-cm signal measurements while accounting rigorously for the uncertainties in foregrounds and high redshift astrophysics. We include the latest publicly available 21-cm power spectrum upper limits from HERA, 21-cm global signal data from SARAS 3, and the synergistic probe of the unresolved X-ray background in our final analysis. This paper thus constitutes the first attempt to use 21-cm power spectrum data to probe cosmic strings. In contrast to previous works, we find no strong constraints can be placed on superconducting cosmic strings from current 21-cm measurements. This is because of uncertainties in the X-ray emission efficiency of the first galaxies, with X-ray emissivities greater than 3×10^{40} erg s^{-1} M$_\odot^{-1}$ yr able to mask the presence of cosmic strings in the 21-cm signal. We conclude by discussing the prospects for future constraints from definitive 21-cm signal measurements and argue that the recently proposed soft photon heating should be cause for optimism due to its potential to break degeneracies that would have otherwise made the signatures of cosmic strings difficult to distinguish from those of astrophysical origin.

Key words: dark ages, reionization, first stars – early Universe – cosmology: observations – X-rays: diffuse background.

1 INTRODUCTION

Many extensions to the standard model predict the existence of cosmic strings. Should cosmic strings exist, they can play a significant role in early structure formation (Brandenberger 1994), a topic receiving renewed attention due to the recent launch of JWST and the detection of overly large galaxies at high redshifts (e.g. Akins et al. 2023; Boylan-Kolchin 2023; Labbé et al. 2023). In addition, cosmic strings may also explain the excess radio background seen by ARCADE 2 and the LWA (Fixsen et al. 2011; Dowell & Taylor 2018; Cyr, Chluba & Acharya 2023a). Hence, any probes of these topological defects allow for the indirect constraint of new physics at high energies and can potentially provide insight into outstanding problems in astrophysics and cosmology.

One promising current and near-future probe is the 21-cm signal from between the cosmic dark ages and reionization. The 21-cm signal measures the excess or deficit of rest-frame 21-cm wavelength photons due to the neutral hydrogen gas present throughout the intergalactic medium in these early epochs (Madau, Meiksin & Rees 1997; Furlanetto, Oh & Briggs 2006; Pritchard & Loeb

2012; Barkana 2016; Mesinger 2019). Through the spatial and time evolution of the 21-cm signal, the formation of the first stars and galaxies is traceable, allowing for insight into early astrophysics (e.g. Yajima & Khochfar 2015; Cohen, Fialkov & Barkana 2016; Mebane, Mirocha & Furlanetto 2018; Mirocha et al. 2018; Tanaka et al. 2018; Schauer, Liu & Bromm 2019; Mebane, Mirocha & Furlanetto 2020; Gessey-Jones et al. 2022; Muñoz et al. 2022; Bevins et al. 2022b) and the nature of dark matter (e.g. Barkana 2018; Fraser et al. 2018; Muñoz, Dvorkin & Loeb 2018; Liu et al. 2019; Jones et al. 2021; Abdurashidova et al. 2022a; Barkana et al. 2023).

Multiple mechanisms have been proposed by which cosmic strings can impact the 21-cm signal. The overdensity produced in the wake of a string enhances the 21-cm signal in a wedge (Brandenberger et al. 2010; Hernández & Brandenberger 2012; Hernández 2014), which should be visible in 21-cm images and three-point statistics (Maibach et al. 2021). Furthermore, a subclass of cosmic strings, those that carry supercurrents (Witten 1985), may enhance the 21-cm signal globally through the emission of an excess radio background (Feng & Holder 2018; Thériault, Mirocha & Brandenberger 2021). This latter effect potentially being of sufficient magnitude to allow for preliminary constraints on superconducting cosmic strings from the disputed EDGES 21-cm signal measurement (Bowman et al.

2018; Hills et al. 2018; Brandenberger, Cyr & Shi 2019; Singh & Subrahmanyan 2019; Sims & Pober 2020).

The field of observational 21-cm cosmology has seen rapid development since the EDGES measurement. With the SARAS 3 global signal null-result (Singh et al. 2022) rejecting the best-fitting EDGES profile at the 95.3 per cent level, and the latest public HERA 21-cm power spectrum upper limits (Abdurashidova et al. 2022b; HERA Collaboration et al. 2023) which are now sufficiently low to be probing the astrophysics of the first galaxies (Abdurashidova et al. 2022a). Combining these global 21-cm signal and 21-cm power spectrum results has proven fruitful, giving stronger constraints on a class of 21-cm models with an excess radio background from high redshift radio galaxies (Bevins et al. 2024). These observations and the subsequent analyses show that existing 21-cm signal measurements are already teaching us much about the early Universe. However, they have also revealed the complex degeneracies that exist between high-redshift astrophysical parameters, foregrounds, and exotic physics, which must be carefully considered before drawing any conclusions from these data sets.

Further insights into the early Universe have come from the unresolved X-ray background (Brandt & Yang 2022), the residual X-ray flux measured by X-ray telescopes after subtraction of resolved point sources. This unresolved background acts as an upper bound on the X-ray flux from high redshift sources, which thus constrains high redshift astrophysical parameters (Fialkov et al. 2017). HERA Collaboration et al. (2023) and Pochinda et al. (2023) have shown that such constraints are complementary to those from the 21-cm signal.

In this paper, we build on the work of Pochinda et al. [2023; an extension of an earlier analysis by Bevins et al. (2024)], whose authors showed that a multiwavelength analysis combining observations of the 21-cm power spectrum (HERA Phase 1 Limits, HERA Collaboration et al. 2023), 21-cm global signal (SARAS 3 null result, Singh et al. 2022), unresolved X-ray background (Hickox & Markevitch 2006; Harrison et al. 2016), and excess radio background (Dowell & Taylor 2018), gave significant insights into early Universe astrophysics, including providing constraints on the properties of galaxies and Population III stars. Instead of focusing on astrophysics, here we investigate the constraints on cosmic strings a joint analysis of the same 21-cm power spectrum, 21-cm global signal, and unresolved X-ray background data can provide. We do not include excess radio background data as our cosmic string model is not valid at $z = 0$. This paper thus constitutes the first analysis to attempt to constrain superconducting cosmic strings using 21-cm power spectrum data.

We first alter the version of 21-cm Semi-numerical Predictions Across Cosmic Epochs (21CMSPACE; Fialkov et al. 2012; Visbal et al. 2012; Fialkov et al. 2013, 2014a; Fialkov, Barkana & Visbal 2014b; Cohen et al. 2016; Fialkov & Barkana 2019; Reis, Fialkov & Barkana 2020, 2021; Gessey-Jones et al. 2022; Magg et al. 2022; Reis, Barkana & Fialkov 2022; Gessey-Jones et al. 2023; Sikder et al. 2024) used in Pochinda et al. (2023) to model an excess radio background from superconducting cosmic strings. Using this code, we generate a data set of 21-cm signal and X-ray background predictions for different astrophysical and cosmic strings scenarios, from which we train emulators for efficient evaluation of these observables. We then employ a Bayesian methodology to allow for the proper marginalization of the foregrounds and the uncertain astrophysics of the early Universe when extracting our constraints on cosmic strings. Ultimately, we determine that astrophysical uncertainties are too great for us to draw any robust conclusions about superconducting cosmic strings from existing 21-cm observations.

During the preparation of this paper, a series of related works (Acharya, Cyr & Chluba 2023; Cyr et al. 2023a, b) were published. These studies propose an intriguing new mechanism *soft photon heating* by which superconducting cosmic strings heat the intergalactic medium, an effect not included in our study. Acharya et al. (2023) find the inclusion of this heating suppresses the amplitude of the 21-cm global signal. As a result, Cyr et al. (2023b) find there to be no constraints on superconducting cosmic strings at 2σ significance when treating the EDGES global signal measurement as a limit on the 21-cm global signal magnitude at $z = 18$. This is in agreement with our conclusions that current 21-cm signal measurements cannot constrain superconducting cosmic strings. However, we reach this conclusion due to the uncertainty in astrophysical heating while their heating is intrinsic to the cosmic strings. Together, our works illustrate the importance of considering all effects, foreground, astrophysical, and from the strings themselves when attempting to constrain cosmic strings using the 21-cm signal. We discuss further how including soft photon heating would impact our conclusions in Section 6.

We begin by recapping the theory of the excess radio background from superconducting cosmic strings in Section 2 and its impact on the 21-cm signal in Section 3. Then we outline the observations we use for our constraints in Section 4 alongside our data analysis methodology. Afterwards, the results from our analysis are presented in Section 5. Finally, we conclude in Section 6, with discussions of our findings and with the prospects for future constraints on superconducting cosmic strings from 21-cm signal measurements.

2 AN EXCESS RADIO BACKGROUND FROM SUPERCONDUCTING COSMIC STRINGS

Throughout this work, we focus on the impact of superconducting cosmic strings on the 21-cm signal via the excess radio background, for which we use the model developed by Brandenberger et al. (2019) and Thériault et al. (2021). Below, we recap the main details of this model. A reader familiar with these works may wish to skip to the next section.

If cosmic strings exist, they will have formed before recombination as the Universe is rapidly cooling post-Big Bang (Brandenberger 1994). As the temperature drops, so does the energy scale of the fields that permeate the Universe. When this energy scale crosses critical values, the nature of the ground state (also called vacuum) of one or more of these fields changes abruptly in what is called a phase transition (Mazumdar & White 2019). If the new ground states no longer have a symmetry present in the old ground state, the transition is a spontaneous symmetry-breaking one. The canonical example of such a transition is the Higgs mechanism, wherein the electroweak gauge symmetry is broken as the Higgs field undergoes a phase transition at an energy scale of 160 GeV (D'Onofrio & Rummukainen 2016).

In a symmetry-breaking phase transition, the new ground states of the field will be a degenerate set. Causality dictates that the first small regions of the new ground state to form will thus be in different degenerate ground states (Kibble 1976, 1980, 1982). These regions of new vacuum grow outward at the speed of light and eventually fill the entire Universe. However, if the topology of the new degenerate ground state is not simply connected (i.e. it has holes), these expanding bubbles of new vacuum cannot smoothly merge into one region all in the same vacuum state. As a result, where the bubbles meet topological defects in the field are left behind, regions where the field is stuck in a higher energy state because the ground state's topology prevents it from relaxing. This process, wherein causality

and ground state topology combine to create topological defects in cosmological fields, is the Kibble mechanism (Kibble 1976).

The nature of the topological defects produced via the Kibble mechanism depends on the specific topology of the new ground states, with possible types of defect including cosmic strings, domain walls, monopoles, and texture (Brandenberger 1994). For example, cosmic strings are produced if the set of new ground states is topologically equivalent to a 1D ring (1-sphere). These cosmic strings are nearly 1D regions where the field is stuck in a higher energy state. As a result, a gauge particle condensate exists along the string, thus giving it gravitational mass. A network of such strings is expected to form via the Kibble mechanism if an appropriate symmetry-breaking phase transition occurs, comprising a mixture of infinite strings permeating the Universe and a smaller number of finite string loops (Vanchurin, Olum & Vilenkin 2006). Since none of the phase transitions in the standard model of particle physics produce cosmic strings, their presence would be a smoking gun sign of physics beyond the standard model, allowing any observations that constrain their potential properties to probe these theories.

If the condensate forming the cosmic strings is charged, which is true for a large subclass of theories, the whole string becomes superconducting (Witten 1985) and so carries a theory-dependent current I. Consequently, superconducting strings lose energy to electromagnetic radiation, in addition to the gravitational radiation losses that all cosmic strings experience. Due to having two competing energy loss mechanisms, superconducting cosmic strings can be split into three categories based on which loss mechanism dominates: supercritical strings that primarily lose energy to electromagnetic radiation; subcritical strings that primarily lose energy to gravitational waves; and critical strings for which the two energy loss mechanisms are of equal magnitude. The critical current that divides these regimes for fixed μ is given by[1]

$$I_c = \kappa^{-1} \gamma G^{-1/2} (G\mu)^{3/2}, \tag{1}$$

where G is Newton's constant, κ a dimensionless electromagnetic emissivity constant of order 1, and γ is another dimensionless constant related to the efficiency of gravitational wave emission (numerical simulations give $\gamma \sim 100$, Vachaspati & Vilenkin 1985). Supercritical strings have $I > I_c$, and subcritical strings have $I < I_c$.

We will assume that all cosmic strings in our model have the same current I and tension μ, and hence all are either supercritical, critical, or subcritical. That is not, however, to say we model all cosmic strings as identical. The phase transition that produced the cosmic strings will have left the strings with a range of loop radii R (e.g. Vilenkin 1981; Albrecht & Turok 1985; Hindmarsh & Kibble 1995), which in the matter-dominated epoch follows the scaling number density

$$n(R, t) = \begin{cases} \chi R^{-5/2} t_{\text{eq}}^{1/2} t^{-2} & \text{for } R_c(t) < R < \psi t_{\text{eq}}, \\ R^{-2} t^{-2} & \text{for } R \geq \psi t_{\text{eq}}, \end{cases} \tag{2}$$

where t is cosmic time, t_{eq} the cosmic time of matter-radiation equality, χ and ψ are model-specific dimensionless constants,[2] and $R_c(t)$ the cutoff radius. The cutoff radius is defined as the radius below which cosmic strings are expected to decay within a Hubble time and so this value is dependent on the dominant energy-loss

mechanism of the cosmic strings

$$R_c(t) = \begin{cases} \kappa \beta^{-1} I \mu^{-1/2} t & \text{for } I > I_c, \\ \kappa \beta^{-1} G\mu t & \text{for } I \leq I_c. \end{cases} \tag{3}$$

Here, β is another dimensionless model-specific parameter, encoding the shape of the loops.[3]

The final piece of information required to calculate the radio background from cosmic strings is their emissivity. Cai, Sabancilar & Vachaspati (2012) calculated the power P emitted per angular frequency ω by superconducting cosmic strings at low frequencies to be

$$\frac{dP}{d\omega} = \kappa I^2 R^{1/3} \omega^{-2/3}. \tag{4}$$

By combining equations (2), (3), and (4), the radio emissivity of the cosmic string population can be found. Radio photons began to be able to freely stream through the Universe at recombination, and so the radio background post-recombination is given by integrating the contribution from cosmic strings back to recombination accounting for the redshifting of photons by the expansion of the Universe. The resulting excess energy density in radio photons below a given angular frequency was found by Brandenberger et al. (2019) to be

$$\rho(t; \omega) = 18\tilde{\kappa} \chi \beta^{7/6} \omega^{1/3} t_{\text{eq}}^{1/2} t^{-13/6}$$
$$\times \begin{cases} \kappa^{-7/6} G^{-7/12} I^{5/6} (G\mu)^{7/12} & \text{for } I > I_c, \\ \gamma^{5/6} \kappa^{-2} G^{-1} (G\mu)^{11/6} & \text{for } I = I_c, \\ \gamma^{-7/6} I^2 (G\mu)^{-7/6} & \text{for } I < I_c, \end{cases} \tag{5}$$

with $\tilde{\kappa}$ being κ multiplied by an order one constant.

Here we are treating the cosmic string background as homogeneous. At the redshifts of interest, this assumption begins to break down at $G\mu \gtrsim 1$ when there is no longer a large number of cosmic string radio bubbles overlapping at every point in space. In this work, we do not consider $G\mu > 10^{-6}$, as these tensions have been ruled out via pulsar timing arrays (Miyamoto & Nakayama 2013). As a result, for our applications, the homogeneity assumption is well justified.

From the above, we can find the superconducting cosmic string produced excess radio temperature at the 21-cm line frequency ω_{21}

$$\Delta T_{\text{rad}}^{21} = 6\pi^2 \tilde{\kappa} \chi \beta^{7/6} \omega_{21}^{-8/3} t_{\text{eq}}^{-5/3} \left(\frac{1+z}{1+z_{\text{eq}}} \right)^{13/4}$$
$$\times \begin{cases} \kappa^{-7/6} G^{-7/12} I^{5/6} (G\mu)^{7/12} & \text{for } I > I_c, \\ \gamma^{5/6} \kappa^{-2} G^{-1} (G\mu)^{11/6} & \text{for } I = I_c, \\ \gamma^{-7/6} I^2 (G\mu)^{-7/6} & \text{for } I < I_c, \end{cases} \tag{6}$$

where we have converted from cosmic time to redshift z, with z_{eq} the redshift of matter-radiation equality. Note our formula differs by a factor of 9 to that of Thériault et al. (2021) due to the authors erroneously converting between ρ and ΔT_{rad} using the formula for black-body radiation. The cumulative energy spectrum from cosmic strings in the radio is a power-law with spectral index 1/3 [e.g. equation (5)] not black-body (approximately a power-law with spectral index 3 at low frequencies), correcting for which results in the difference in the numeric factor.

21CMSPACE, discussed in the next section, can model a spatially homogeneous excess radio background at the rest-frame 21-cm line

---

[1]All equations in this section are given in natural units, $c = k_{\text{B}} = \hbar = 1$.
[2]The χ and ψ constants here were called ν and α in Brandenberger et al. (2019) but are renamed here to avoid confusion in subsequent sections with frequency and X-ray spectral index respectively.

[3]2π for circular loops.

of the form (Fialkov & Barkana 2019; Reis et al. 2020)[4]

$$\Delta T_{\rm rad}^{21} = T_{\rm cmb,0}(1 + z)\left(A_{\rm r}[1 + z]^{B_{\rm r}}\right), \qquad (7)$$

with $T_{\rm cmb,0}$ being the cosmic microwave background temperature seen today. By comparison to the theoretical prediction for the radio background above, we see they are of the same form if we define the relative magnitude of this excess to be

$$A_{\rm r} = 6\pi^2 \tilde{\kappa} \chi \beta^{7/6} \omega_{21}^{-8/3} t_{\rm eq}^{-5/3} T_{\rm cmb,0}^{-1} (1 + z_{\rm eq})^{-13/4}$$
$$\times \begin{cases} \kappa^{-7/6} G^{-7/12} I^{5/6} (G\mu)^{7/12} & \text{for } I > I_{\rm c}, \\ \gamma^{5/6} \kappa^{-2} G^{-1} (G\mu)^{11/6} & \text{for } I = I_{\rm c}, \\ \gamma^{-7/6} I^2 (G\mu)^{-7/6} & \text{for } I < I_{\rm c}, \end{cases} \qquad (8)$$

and the exponent of its redshift evolution as

$$B_{\rm r} = 9/4. \qquad (9)$$

This $A_{\rm r}$ formalism has the added advantage of condensing all of the degenerate model-specific parameters, β, γ, κ, $\tilde{\kappa}$, χ, μ, and I into one. Thus, we can, and will, constrain the phenomenological radio background strength $A_{\rm r}$ and later convert these constraints to any superconducting cosmic string model of interest.

A homogeneous radio background also described by equation (7) has been previously constrained using 21-cm signal data in Abdurashidova et al. (2022a) and Bevins et al. (2022b), using an earlier set of HERA Phase 1 21-cm power spectrum upper limits, and the SARAS 3 21-cm global signal data, respectively. With both finding higher excess radio, background magnitudes were disfavoured but not ruled out by their respective data sets. However, in those studies, the background was assumed to be from synchrotron radiation and a value of $B_{\rm r} = 2.6$ was used,[5] rather than the value of 2.25 that we consider here. Hence, we would expect the radio backgrounds from cosmic strings to have a smoother evolution than that used in those studies, decaying away less rapidly. As a result, the two types of radio backgrounds will have distinct impacts on the time evolution of the 21-cm signal, thus requiring us to perform a separate analysis rather than reinterpreting the results from these earlier studies.

We should re-emphasize here for clarity that the above equations assume a matter-dominated epoch. This is a good approximation for the period of the Universe's history that the 21-cm signal is sensitive to ($5 < z < 150$). However, the approximation breaks down at lower redshifts and no longer holds at $z = 0$ due to the effects of dark energy. Thus, we cannot use the derived equations to rigorously constrain superconducting cosmic strings using the present-day excess radio background measured by ARCADE 2 and the LWA (Fixsen et al. 2011; Dowell & Taylor 2018). If

we were to assume, equation (6) holds down to $z = 0$, then the excess radio background measurements listed in Dowell & Taylor (2018) rule out $A_{\rm r} \gtrsim 0.1$. Since we do not anticipate significant deviations from equation (6) for the complete ΛCDM calculation, this figure can be treated as illustrative of the order of magnitude of constraints on $A_{\rm r}$ from ARCADE 2 and LWA. But, as this figure is only approximate, we do not use it as part of our constraints or consider the present-day radio background further in this work. While this paper was in preparation, Cyr et al. (2023b) published a thorough analysis constraining the parameters of superconducting cosmic strings using present-day radio background measurements, including a full modelling of ΛCDM cosmology and a more detailed radiative transfer treatment than is used here.

3 IMPACTS OF AN EXCESS RADIO BACKGROUND ON THE 21-CM SIGNAL

The 21-cm signal is the change in abundance of rest-frame 21 cm wavelength photons relative to a radio background caused by the presence of neutral hydrogen in the early Universe (Furlanetto et al. 2006). Normally, this signal is expressed as the difference in radio brightness temperature observed today T_{21}. Due to the expansion of the Universe, the differential brightness temperature at different frequencies probes different epochs of the history of the Universe. The strength of the signal observed depends on the optical depth of the 21-cm line τ_{21}, the temperature of the radio background $T_{\rm rad}$ and the spin temperature of the observed patch of hydrogen gas $T_{\rm s}$ as

$$T_{21} = \left(1 - e^{-\tau_{21}}\right) \frac{T_{\rm s} - T_{\rm rad}}{1 + z}. \qquad (10)$$

$T_{\rm s}$ is a statistical temperature encompassing the relative occupation of excited and non-excited states of neutral hydrogen. Thus the relative values of $T_{\rm s}$ and $T_{\rm rad}$ determine whether the hydrogen gas is a net emitter or absorber of 21-cm photons, and hence the sign of T_{21}.

From equation (10), it can immediately be seen that enhancing the radio background $T_{\rm rad}$ would have an impact on the 21-cm signal (Ewall-Wice et al. 2018; Feng & Holder 2018; Fialkov & Barkana 2019; Reis et al. 2020). However, $T_{\rm s}$ also depends on $T_{\rm rad}$. $T_{\rm s}$ is determined by the competing influences of absorption/emission of radiation from the background, collisions of neutral hydrogen, and the Wouthuysen–Field effect (Wouthuysen 1952; Field 1958). The first of which forces $T_{\rm s}$ toward $T_{\rm rad}$, while the other two force it towards the kinetic temperature of the neutral hydrogen gas. Hence, a full picture of how the 21-cm signal depends on $T_{\rm rad}$ needs to account for the relative strength of these three processes, which will vary in both time and space.

To accurately calculate the dependence of the 21-cm signal on $A_{\rm r}$, we utilize our pre-existing simulation code 21CMSPACE.[6] The code follows a seminumerical paradigm, with small-scale physics (e.g. star formation) handled by analytic prescriptions, and large-scale physics (e.g. radiative transfer) modelled numerically. This hybrid approach speeds up the code considerably compared to numerical simulations, allowing each simulation to complete in a few hours. Within the simulation itself, the Universe is modelled as a periodic box, divided into 128^3 cells, each with side length 3 comoving Megaparsecs (cMpc). As a result, the code ultimately produces 3D maps of the 21-cm signal at this resolution across the range of redshifts the simulation is run between, in our case $z = 50$ to 6.

---

[4]In some previous works (Fialkov & Barkana 2019; Reis et al. 2020), $A_{\rm r}$ was defined as the magnitude of the excess radio background relative to the CMB at $z = 17.2$, rather than at $z = 0$. Hence, there is a numeric factor difference of $18.2^{B_{\rm r}}$ between the $A_{\rm r}$ convention in these works and ours. For $B_{\rm r} = 2.25$, this numeric factor is 684, thus, the limit on $A_{\rm r}$ required to replicate the depth of the EDGES signal found in Fialkov & Barkana (2019) corresponds to $A_{\rm r} \gtrsim 0.0028$ in our notation.

[5]The value of 2.6 used in Abdurashidova et al. (2022a) and Bevins et al. (2022b) was motivated by the measurement of the spectral index of the present-day excess radio background by Dowell & Taylor (2018), 2.58 ± 0.05. In the same work, the spectral index of galactic synchrotron radiation was found to vary from 2.48 to 2.62 across the sky. So, while there is some uncertainty, or intrinsic variation, in the spectral index of synchrotron radiation its value is larger than the $B_{\rm r}$ value predicted for superconducting cosmic strings.

[6]For a detailed up-to-date description of the code and its latest features, see Gessey-Jones et al. (2023).

However, current 21-cm signal experiments do not aim to produce 21-cm tomographic maps but instead, attempt to observe summary statistics of the 21-cm signal that are easier to measure. They target either the sky-averaged 21-cm global signal $\langle T_{21}\rangle(z$; Bowman et al. 2018; Philip et al. 2019; de Lera Acedo et al. 2022; Singh et al. 2022; Monsalve et al. 2023) or the 21-cm power spectrum $\Delta^2(z, k$; Ewall-Wice et al. 2016; Mertens et al. 2020; Mertens, Semelin & Koopmans 2021; Abdurashidova et al. 2022b). Consequently, we similarly compress the outputs of all our simulations into these summary statistics. Both these summary statistics depend on the redshift being observed z and so probe the time evolution of the 21-cm signal. Additionally, the 21-cm power spectrum probes the spatial evolution of the 21-cm signal through the fluctuations at different scales set by the wavenumber k.

Much about the early Universe remains uncertain, and so, 21CMSPACE has various parameters and settings that describe or enable astrophysical and cosmological processes. For all simulations used in this study, we include modelling of:

(i) Baryon dark-matter relative velocities (Fialkov et al. 2012; Visbal et al. 2012)

(ii) Wouthuysen–Field effect (Fialkov et al. 2013)

(iii) Ly α multiple scattering (Reis et al. 2021)

(iv) Ly α heating (Reis et al. 2021)

(v) CMB heating (Venumadhav et al. 2018; Fialkov & Barkana 2019)

(vi) X-ray heating including SED dependance (Pacucci et al. 2014; Fialkov et al. 2014b)

(vii) Reionization (Fialkov et al. 2014b)

(viii) Photoheating feedback (Cohen et al. 2016)

(ix) Lyman–Werner feedback (Fialkov et al. 2013; Muñoz et al. 2022)

(x) Population III (Pop III) star to population II (Pop II) transition (Magg et al. 2022)

(xi) Pop III star initial mass function (IMF, Gessey-Jones et al. 2022)

(xii) Star formation efficiency suppression in low-mass haloes (Fialkov et al. 2013)

We fix the maximum root mean free path of ionizing photons to 40 cMpc and the Pop III star initial mass function to a logarithmically flat IMF between 2 and 180 $M_\odot$ (Klessen & Glover 2023), as they are found to have little impact on our results. We assume galaxies do not contribute to the radio background so that there is only one source of excess radio background in our simulations. Constraining models with multiple sources of excess radio background is left to future works. The remaining free parameters of the code allow us to explore different scenarios for the uncertain astrophysical properties of the early Universe. Specifically, we can vary the excess radio background strength A_r (see previous section), star formation efficiency of Pop II, $f_{*,\,II}$, and Pop III, $f_{*,\,III}$, stars, the delay time between the two stellar populations, t_{delay}, the X-ray emission efficiency of galaxies, f_X, the X-ray spectrum of galaxies described by a spectral index α and low-energy cutoff E_{min}, the critical circular velocity for stars to form in a halo, V_c, and the efficiency of galaxies at emitting ionizing photons, ζ.

We utilize the same version of 21CMSPACE as Pochinda et al. (2023), but we model a superconducting cosmic string radio background in our simulations rather than an excess radio background from galaxies. A detailed discussion of the changes to 21CMSPACE from the version commonly employed in older analyses (Abdurashidova et al. 2022a; Bevins et al. 2022c; HERA Collaboration et al. 2023; Bevins et al. 2024) is provided in that paper. However,

for clarity, we here summarize the relevant improvements to the code. Star formation is now modelled following the prescription introduced by Magg et al. (2022), separating Pop II and Pop III star formation. Hence, haloes are now assumed to first form Pop III stars with efficiency $f_{*,\,III}$ once they cross the critical mass threshold for star formation. Then the halo takes a time t_{delay} to recover from the ejection of material by Pop III star supernovae, after which it can begin forming Pop II stars with efficiency $f_{*,\,II}$. Each of the stellar populations has a separate Lyman band spectra, in the Pop III case, this is derived from the Pop III IMF (Gessey-Jones et al. 2022), while for Pop II stars, a fixed spectrum from Leitherer et al. (1999) is used.[7] Finally, a module that calculates the X-ray background from high redshift sources has been added to 21CMSPACE, following the methodology from Fialkov et al. (2017).

For self-consistency, this new X-ray background module calculates the contribution of high-redshift sources to the present-day unresolved X-ray background in a similar manner to which X-ray heating is modelled within 21CMSPACE (Fialkov et al. 2014a). Hence, it also assumes that star-forming haloes are X-ray sources with a starburst galaxy-like luminosity to star formation rate relation (e.g. Grimm, Gilfanov & Sunyaev 2003; Mineo, Gilfanov & Sunyaev 2012)

$$L_X = \left(3\times 10^{40}\ \text{erg}\ \text{s}^{-1}\ M_\odot^{-1}\ \text{yr}\right) f_X \text{SFR}, \qquad (11)$$

where SFR is the star formation rate of the halo and $f_X = 1$ corresponds to the specific luminosity predicted by Fragos et al. (2013) for low metallicity X-ray binaries. The SED of these X-ray sources is assumed to be a power-law with lower cutoff energy E_{min} and power-law slope α. By combining the above with the simulated star formation rate density, 21CMSPACE is then able to compute the specific X-ray emissivity $\epsilon_X(z, E)$ throughout the simulation. The present-day specific intensity from $z \geq 6$ sources can then be calculated in the simulation using (e.g. Pritchard & Furlanetto 2007)

$$J_X(E) = \frac{c}{4\pi}\int_{z'=6}^{\infty}\epsilon_X\left(z', E(1+z')\right)\frac{e^{-\tau_X(z', E)}}{(1+z')H(z')}dz', \qquad (12)$$

where H is the Hubble parameter, E the X-ray energy, and $\tau_X(z', E)$ is the optical depth of X-rays between their emission redshift of z' and the present day. $\tau_X(z', E)$ is, in turn, calculated by integrating the X-ray cross-section of hydrogen and helium species[8] in the IGM between z' and $z = 0$ (Verner et al. 1996). $J_X(E)$ is now a standard output of 21CMSPACE simulations to facilitate comparisons, like those we perform in this paper, of models of the early Universe to the observed unresolved X-ray background data.

By fixing the astrophysical parameters and running simulations varying the strength of the excess radio background A_r, we can gain an intuition for the impacts of the presence of superconducting cosmic string on the 21-cm signal. We illustrate 21-cm signals with A_r varying between 10^{-6} and 10^3 for fixed $f_{*,\,II} = 0.05$, $f_{*,\,III} = 0.002$, $t_{delay} = 30$ Myr, $f_X = 1$, $\alpha = 1.5$, $E_{min} = 200$ eV, $V_c = 5.6$ km s^{-1}, and $\zeta = 15$ in Fig. 1. Concentrating first on the global 21-cm signal, we observe that as A_r increases, the 21-cm global signal absorption trough becomes deeper, ranging from 100 to 900 mK. Depending on the astrophysical parameters chosen, the signal depth

---

[7]Currently, Pop II and Pop III star-forming haloes are assumed to have the same X-ray emission efficiency f_X and SED in our models. This assumption is not anticipated to strongly impact our constraints on A_r, and hence on cosmic strings.

[8]The contribution of metals is assumed to be small due to their lower abundance.
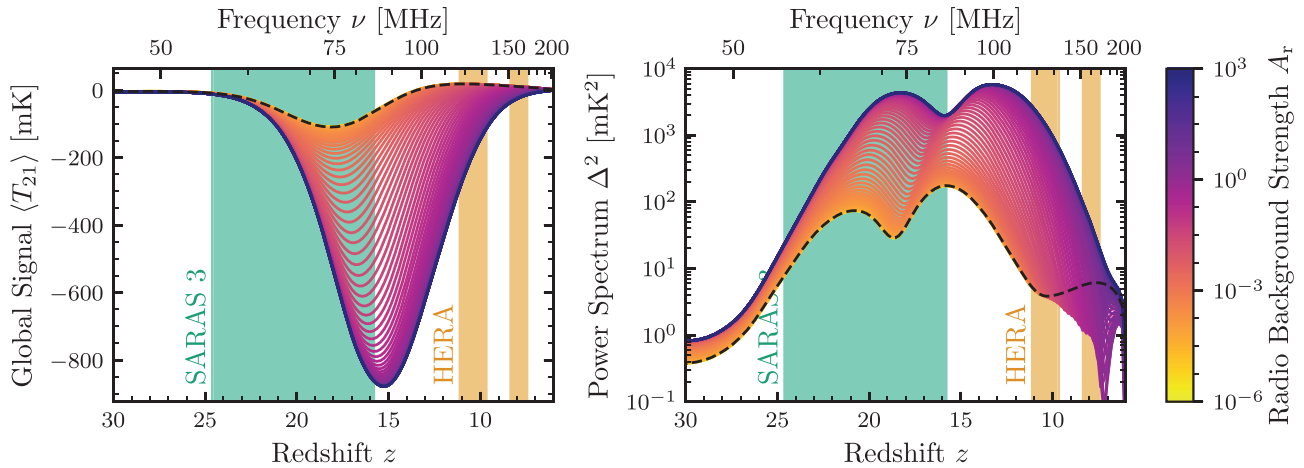
Figure 1. Variation of the 21-cm global signal (left) and 21-cm power spectrum (right) with the strength of the excess radio background. The 21-cm power spectrum is shown for $k = 0.34\,h\,\mathrm{cMpc}^{-1}$ $(0.23\,\mathrm{cMpc}^{-1})$. All astrophysical parameters are the same between the depicted signals, and the 21-cm signal when there is no excess radio background (e.g. CMB only) is shown as a black dashed line. The SARAS 3 band is illustrated in green and the HERA bands are in orange. An increase in the excess radio background is seen to increase the magnitude of the global signal absorption trough (100–900 mK) and move it later ($z = 18$–15), in this case outside of the SARAS 3 band. Similar effects occur in the 21-cm power spectrum, with the power spectrum magnitude increasing with A_r and the cosmic dawn and heating peaks shifting to later times. At very high $A_r \gtrsim 10^1$ and very low $A_r \lesssim 10^{-4}$ values of the radio background strength the signal is seen to saturate and no further variation is observed. In the case of very low $A_r \lesssim 10^{-4}$, the signals become visually indistinguishable from the 21-cm signal with no excess radio background.

under an excess radio background can be up to several Kelvin (for an example, see Fig. A3). However, this growth is not endless since the signal magnitude eventually saturates (Reis et al. 2020); in the illustrated case, this occurs at $A_r \gtrsim 10^1$. The fundamental cause of this saturation is the balance between the couplings that determine T_s. At very high A_r the radiative coupling dominates, causing T_s to become approximately proportional to $T_{\rm rad}$, and since $\tau_{21} \propto T_s^{-1}$ then in this limit $\tau_{21} \propto T_{\rm rad}^{-1}$. Hence, the $T_{\rm rad}$ dependence of the bracketed term in equation (10) and the numerator cancel in the high A_r and $T_{\rm rad}$ limit, leading to a 21-cm signal that no longer depends on $T_{\rm rad}$ or A_r (see Fialkov & Barkana 2019, for the exact limit). Conversely, if the excess radio background is much smaller than the CMB, then it has negligible impact on the 21-cm signal as is seen for $A_r \lesssim 10^{-4}$, and so the 21-cm signal is insensitive to A_r in the low A_r limit as well. One final impact of increasing A_r is that the global signal minimum shifts to later times (lower redshifts), this is potentially important to our study as it can move the global signal minima outside the SARAS 3 band (see Section 4.2), as shown in the figure, making the signal harder to distinguish from the smooth galactic foregrounds.

We observe similar trends in the $k = 0.34\,h\,\mathrm{cMpc}^{-1}$ 21-cm power spectrum.[9] Like the magnitude of the global signal absorption trough, the magnitude of the 21-cm power spectrum grows with A_r but saturates at both low and high A_r values. In addition, as A_r increases, the cosmic dawn and X-ray heating peaks in the power spectrum move to later times. Hence, an excess radio background from superconducting cosmic strings can have considerable impacts on the 21-cm signal, suggesting it may be possible to extract constraints on superconducting cosmic strings from existing 21-cm signal data. We now describe said 21-cm signal data as well as that from complementary probes of the early Universe that we will use in our joint analysis.

---

[9]h is the Hubble parameter normalized by $100\,\mathrm{km\,s}^{-1}\,\mathrm{Mpc}^{-1}$, for which throughout we assume the *Planck* 2018 (Planck Collaboration 2020) best-fitting value for h of 0.674. The stated wavenumber is thus equivalent to $0.23\,\mathrm{cMpc}^{-1}$.

4 DATA SETS AND METHODOLOGY

In previous studies, Bevins et al. (2024) demonstrated that a joint analysis of 21-cm global signal and power spectrum data was able to constrain the properties of the first galaxies, while HERA Collaboration et al. (2023) and Pochinda et al. (2023) showed that high-redshift astrophysical constraints could be further improved by including information on the unresolved X-ray background. Motivated by these works, we use a joint analysis of 21-cm global signal, 21-cm power spectrum, and unresolved X-ray background data for our constraints on superconducting cosmic strings, all three of which can be modelled self-consistently by 21CMSPACE. We begin this section by introducing these three sets of observations in Sections 4.1, 4.2, and 4.3, before detailing our data analysis methodology in Section 4.4.

4.1 HERA

The Hydrogen Epoch of Reionization Array (HERA) is a radio interferometer designed to detect the 21-cm power spectrum (Abdurashidova et al. 2022b). It is currently in operation, and the collaboration behind the experiment recently published upper limits on the 21-cm power spectrum based on Phase 1 of their observations. Their best current published limits, from 94 nights of observations (HERA Collaboration et al. 2023), were $\Delta^2 \leq 457\,\mathrm{mK}^2$ at $k = 0.34\,h\,\mathrm{cMpc}^{-1}$ and $z = 7.9$, and $\Delta^2 \leq 3496\,\mathrm{mK}^2$ at $k = 0.36\,h\,\mathrm{cMpc}^{-1}$ and $z = 10.4$. An earlier set of limits published by HERA from 18 nights of observations (Abdurashidova et al. 2022b) were at the time the most-constraining published power spectrum limits on permitted early Universe scenarios (Bevins et al. 2024), able to rule out a range of astrophysical and new physics scenarios. Hence, we expect the latest limits, which we use in this study, to similarly provide moderate constraints on our astrophysical parameters, and potentially A_r.

As HERA employs a foreground avoidance strategy, these limits are directly on the 21-cm power spectrum, and so no foreground modelling is needed to extract constraints from them. However, there is the potential for residual systematics in the limits leading to excess

power above thermal noise. We account for such systematics in the same manner as HERA Collaboration et al. (2023) through the form of our likelihood, discussed further in Section 4.4. We are thus inheriting the assumption that residual systematics can only add power, which may not be the case (e.g. Kolopanis et al. 2019). Known sources of signal loss were corrected for in the computation of the HERA upper limits.

4.2 SARAS 3

The Shaped Antenna measurement of the background RAdio Spectrum (SARAS) experiments (Singh et al. 2018, 2022) are a series of radiometers targeting a detection of the global 21-cm signal. SARAS 3 is the most recent in the series, a monopole antenna deployed on a lake in Southern India for 14 d and operating in the 43.75–87.5 MHz frequency range. The experiment was the first of its type to be deployed on a body of water, with this change being made to boost the antenna's overall efficiency and provide a well-characterized uniform medium under the antenna.

We use 15 h of data from the SARAS3 antenna. These data have been pre-processed to calibrate the receiver and antenna bandpass, correct for thermal emission from the water below the antenna, and remove radio frequency interference. The resulting science data set covers 55–85 MHz (redshift 15.7–24.8) in 470 frequency bins and should consist of a combination of time-averaged foregrounds, the global signal and residual noise. Previous studies have shown the SARAS 3 foregrounds are well fit by a 7-coefficient polynomial, with a joint fit of a 21-cm signal model and this foreground model able to refute the best-fitting EDGES measurement at the 95.3 per cent level (Singh et al. 2022) and rule out a large swathe of models with enhanced radio backgrounds from galaxies or synchrotron emission (Bevins et al. 2022b). We hence adopt a similar approach of jointly fitting our 21-cm global signal predictions alongside a 7-coefficient polynomial foreground model to the data.

4.3 Cosmic X-ray background

The cosmic X-ray background is the unresolved X-ray flux detected by X-ray astronomy experiments (see Brandt & Yang 2022, for a recent overview), calculated by subtracting all known sources from the total flux measured by these experiments. As observation times increased and the angular resolution of X-ray telescopes improved, more X-ray point sources have been resolved (Hickox & Markevitch 2006). Consequently, the level of the unresolved background has decreased over time. The remaining unaccounted-for flux should be from a combination of still unresolved point sources (Harrison et al. 2016) and diffuse emission.

Except for the brightest quasars (e.g. Medvedev et al. 2020), X-ray sources from the epoch of reionization, such as X-ray binaries, are too small and faint to be resolved. As a result, the redshifted emission of these sources that survives until today will form a part of the unresolved cosmic X-ray background. Hence, measurements of the X-ray background provide upper limits on the X-ray emissivity of these sources, and thus, another way to constrain high redshift astrophysics (Fialkov et al. 2017).

HERA Collaboration et al. (2023) and Pochinda et al. (2023) find cosmic X-ray background constraints complement 21-cm signal constraints well, ruling out different regions of the astrophysical parameter space. So, we also use unresolved X-ray background measurements (Harrison et al. 2016) from the *Chandra* (Hickox & Markevitch 2006), *HEAO-1* (Marshall et al. 1980; Gruber et al. 1999), *BeppoSAX* (Frontera et al. 2007), *INTEGRAL* (Churazov et al. 2007),

Table 1. Collated measurements of the integrated unresolved cosmic X-ray background from Hickox & Markevitch (2006) and Harrison et al. (2016). These measurements are of the total X-ray flux seen by experiments minus the contribution from known sources. Hence, they act as upper limits on the X-ray background from high redshift sources and so can be used to constrain our models of early Universe astrophysics.

Band (keV)	Measurement $\left[\text{erg cm}^{-2}\text{ s}^{-1}\text{ deg}^{-2}\right]$
1–2	$(1.04 \pm 0.14) \times 10^{-12}$
2–8	$(3.4 \pm 1.7) \times 10^{-12}$
8–24	$(1.832 \pm 0.042) \times 10^{-11}$
20–50	$(2.0 \pm 0.083) \times 10^{-11}$

and *SWIFT* (Ajello et al. 2008) satellites in our joint constraints. We list the values used in Table. 1.

4.4 Bayesian analysis methodology

For our analysis, we follow a Bayesian methodology similar to that of Bevins et al. (2024) and Pochinda et al. (2023). In said methodology, our *a priori* belief in the probability of different parameter values being true $P(\theta)$ is updated by the likelihood of observing some data D given said parameters $P(D|\theta)$ to give us the *a posteriori* probability of different parameter values being true $P(\theta|D)$, via Bayes' theorem

$$P(\theta|D) = \frac{P(D|\theta)P(\theta)}{P(D)}. \tag{13}$$

where $P(D)$ is the Bayesian evidence

$$P(D) = \int P(D|\theta)P(\theta)d\theta. \tag{14}$$

As is typical in Bayesian analyses for brevity, we denote the quantities in equation (13) as the prior $\pi(\theta) = P(\theta)$, the likelihood $\mathcal{L}(\theta) = P(D|\theta)$, the posterior $\mathcal{P}(\theta) = P(\theta|D)$, and the evidence $\mathcal{Z} = P(D)$.

In this study, we are principally interested in the constraints we can extract on superconducting cosmic strings, and hence on A_r. The parameters describing uncertain high redshift astrophysics (θ_a) or foregrounds (θ_f) are considered nuisance parameters in this work. One advantage of adopting a Bayesian approach is we can marginalize over such nuisance parameters to recover the posterior on A_r alone

$$\mathcal{P}(A_r) = \frac{1}{\mathcal{Z}} \int \mathcal{L}(A_r, \theta_a, \theta_f)\pi(A_r, \theta_a, \theta_f)d\theta_a d\theta_f, \tag{15}$$

where we have expanded the previously general θ into three classes of parameters. In practice, to evaluate $\mathcal{P}(A_r)$, we use the slice-sampling-based nested sampling implementation POLYCHORD (Handley, Hobson & Lasenby 2015a, b). As a bonus, this approach also allows us to extract astrophysical constraints discussed in more detail in Appendix A. To fully define equation (15), we hence need to specify $\mathcal{L}(A_r, \theta_a, \theta_f)$ and $\pi(A_r, \theta_a, \theta_f)$. Let us begin with $\mathcal{L}$.

We adopt the same form for the likelihood of HERA 21-cm power spectrum observations as was used in Abdurashidova et al. (2022a)

$$\mathcal{L}_{\text{HERA}}(A_r, \theta_a) \propto \prod_i^n \frac{1}{2}\left(1 + \text{erf}\left[\frac{d_i - m_i(A_r, \theta_a)}{\sqrt{2(\sigma_{d,i}^2 + \sigma_{m,i}^2)}}\right]\right). \tag{16}$$

Above erf is the error function, n the number of data points, m_i the model prediction for the power spectrum at the relevant redshift and wavenumber, $\sigma_{d,i}$ the standard deviation of the measured power spectrum d_i, and $\sigma_{m,i}$ an optional theory model term. This form is

derived from assuming that each independent data point measured d_i is composed of the true signal plus an unknown systematic u_i, then marginalizing away the systematic dependence over a uniform prior. Since the neighbouring wavenumber bins of HERA overlap to ensure this assumption of independent data points is valid, we only include every other wavenumber bin in our analysis starting with the lowest.

As integrated X-ray background observations act as upper limits on the X-ray background from high redshift sources, we follow the methodology of Pochinda et al. (2023) and adopt the same form as equation (16) for the X-ray background likelihood $\mathcal{L}_{\mathrm{X-ray}}$. The independent data points are now the integrated X-ray background in the four bands outlined in Table. 1.

The SARAS 3 data include a foreground from galactic radio emission, which is several orders of magnitude larger than the 21-cm signal. These foregrounds are anticipated to be smooth and so should be well-modelled by a low-order log-log polynomial. As was done in Singh et al. (2022) and Bevins et al. (2022b), we model the foreground radio temperature T_{fg} as a 7-coefficient log-log polynomial of frequency ν

$$\log_{10}\left[\frac{T_{\mathrm{fg}}(\nu)}{1\,\mathrm{K}}\right] = \sum_{i=0}^{i=6} a_i \left(f_{\mathcal{N}}\left[\log_{10}\left(\frac{\nu}{1\,\mathrm{MHz}}\right)\right]\right)^i, \tag{17}$$

where $f_{\mathcal{N}}$ is a linear normalization to map the $\log_{10}(\nu/1\,\mathrm{MHz})$ values between -1 and 1, and the a_i parameters are the foreground coefficient that we treat as nuisance parameters, referred to as a collective as θ_{f}. We thus model the sky-averaged radio temperature as a combination of $T_{\mathrm{fg}}(\nu; \theta_{\mathrm{f}})$ and the global 21-cm signal $T_{21}(\nu; A_{\mathrm{r}}, \theta_{\mathrm{a}})$ predicted by simulations. The noise on the SARAS 3 data is assumed to be Gaussian (Singh et al. 2022) with a standard deviation σ, which we will also fit as nuisance parameters. Hence, the resulting form for the SARAS 3 likelihood we reach is

$$\mathcal{L}_{\mathrm{SARAS}}(A_{\mathrm{r}}, \theta_{\mathrm{a}}, \theta_{\mathrm{f}}) = \prod_j^l \frac{1}{\sqrt{2\pi\left(\sigma^2 + \sigma_{\mathrm{th}}^2\right)}}$$
$$\times \exp\left(-\frac{1}{2}\left[\frac{T_{\mathrm{obs},j} - T_{\mathrm{fg}}(\nu_j; \theta_{\mathrm{n}}) - T_{21}(\nu_j; A_{\mathrm{r}}, \theta_{\mathrm{n}})}{\sigma^2 + \sigma_{\mathrm{th}}^2}\right]^2\right). \tag{18}$$

Here we are taking the product over the l SARAS 3 observed frequencies ν_j, with corresponding observed sky temperature $T_{\mathrm{obs},j}$. We also include an optional theory error term σ_{th} to take into account modelling uncertainties.

Constraints for individual experiments are thus found by using the appropriate likelihood for $\mathcal{L}$ in equation (15). Since the data sets considered are statistically independent-, we can also simply perform joint analyses by taking $\mathcal{L}$ to be the product of the likelihoods we want to include. So for our full joint analysis,

$$\mathcal{L}(A_{\mathrm{r}}, \theta_{\mathrm{a}}, \theta_{\mathrm{f}}) = \mathcal{L}_{\mathrm{HERA}}(A_{\mathrm{r}}, \theta_{\mathrm{a}})$$
$$\times \mathcal{L}_{\mathrm{SARAS}}(A_{\mathrm{r}}, \theta_{\mathrm{a}}, \theta_{\mathrm{f}}) \times \mathcal{L}_{\mathrm{X-ray}}(A_{\mathrm{r}}, \theta_{\mathrm{a}}). \tag{19}$$

An individual nested sampling run can require millions of likelihood evaluations,[10] each of which would naïvely call 21CMSPACE. As the code takes a couple of hours to execute, this would be prohibitively slow. To avoid this problem, we use neural network emulators of 21CMSPACE to reduce the evaluation time of the likelihood to tens of milliseconds, making our nested sampling runs

[10]For example, our joint constraints run performed 130 million likelihood evaluations.

possible in a reasonable time frame. Since we are considering a model with a superconducting cosmic string radio background, which is different to the models used in previous studies, we need to train new emulators for our application. We hence ran 44 836 simulations of the early Universe with randomly sampled A_{r} and astrophysical parameters, the outputs of which are split to form the training and testing set for the emulators of each of our three observables.

We employ the TENSORFLOW (Abadi et al. 2015) based GLOB-ALEMU (Bevins et al. 2021) as the basis for our global signal emulator, using five dense hidden layers of size 32, early-stopping to avoid overfitting, and a 1–10 test-train split. The training data used spanned $z = 6$–28, covering both the SARAS 3 and HERA bands. Once trained, the emulator had an average root-mean-square error of 25 mK for the test data set, which is sufficient for our purposes as the global 21-cm signals we anticipate the SARAS 3 data may be able to rule out are of order 1000 mK (Bevins et al. 2024).

Our power spectrum and X-ray background emulators are derived from the power spectrum emulator developed for Abdurashidova et al. (2022a) and described in Appendix B. thereof. They are implemented using the multilayer perceptron regression neural network from SCIKIT-LEARN (Pedregosa et al. 2011), adopting a GLOBALEMU style methodology of taking as inputs to the network the redshift z and wavenumber k to evaluate the power spectrum at, or energy E to evaluate the X-ray background at. The training and testing data sets covered $z = 6$–28 and $k = 0.085$–$1.000\,\mathrm{cMpc}^{-1}$ for the power spectrum emulator, and $E = 0.40$–$55.00\,\mathrm{keV}$ for the X-ray background emulator. Both networks have four hidden layers of size 100 and a 1–10 test-train split. The converged power spectrum emulator had a relative accuracy of 17 per cent at the 95 per cent percentile, comparable to Abdurashidova et al. (2022a), whereas the X-ray background emulator had a 95 per cent percentile relative accuracy of 5 per cent.

For the inputs to our emulators, instead of using the phenomenological ionizing efficiency of galaxies ζ which is input into 21CMSPACE, we used the derived optical depth to reionization τ output by the simulations. This change was made due to the easier interpretability on τ and existing constraints on τ from *Planck* (Planck Collaboration 2020) allowing for more reasonable priors on its value.

To account for the aforementioned small emulator errors in our analysis, we include a fractional theory/emulator error term $\sigma_{\mathrm{m},i} = 0.17m_i$ in $\mathcal{L}_{\mathrm{HERA}}$, and $\sigma_{\mathrm{m},i} = 0.05m_i$ in $\mathcal{L}_{\mathrm{X-ray}}$. While for the global-signal emulator, we use a frequency-independent theory/emulator error term of $\sigma_{\mathrm{th}} = 25$ mK. This conservative approach should ensure our results are robust to any imprecisions introduced due to using an emulator rather than 21CMSPACE directly.

Finally, we need to define $\pi(A_{\mathrm{r}}, \theta_{\mathrm{a}}, \theta_{\mathrm{f}})$ to fully specify our problem. We place independent priors on each of our parameters as detailed in Table 2. In all of our constraints, we include the A_{r} and *Astrophysical* parameters, whereas the *SARAS* parameters are only needed when the SARAS 3 data forms part of the constraint. The τ prior is derived from the *Planck* 2018 3σ constraints (Planck Collaboration 2020). For the SARAS 3 parameters, we have used priors zoomed in around the best-fitting values of Bevins et al. (2024). We expect the values of the foreground parameters to change little between their work and ours, since Bevins et al. (2024) found that their astrophysical parameters and foreground parameters are uncorrelated, as well as due to the large-scale difference between foreground and signal. As we are only interested in the shape of the posteriors and not the Bayesian evidence, this zooming in does not affect our final results and acts to reduce the Kullback–Leibler (KL) divergence between prior and posterior reducing the nested sampling runtime (Ashton

Table 2. Parameter priors used in our analysis. A_r and the astrophysical parameters are used in all our constraints, whereas the SARAS parameters are only included when the SARAS 3 data are a part of the constraint.

Type	Parameter	Prior	Minimum	Maximum
A_r	A_r	Log-Uniform	10^{-6}	10^3
Astrophysical	$f_{*,\mathrm{II}}$	Log-Uniform	10^{-3}	0.5
	$f_{*,\mathrm{III}}$	Log-Uniform	10^{-3}	0.5
	t_delay	Log-Uniform	10 Myr	100 Myr
	f_X	Log-Uniform	10^{-3}	10^3
	α	Uniform	1	1.5
	E_min	Log-Uniform	0.1 keV	3 keV
	V_c	Log-Uniform	$4.2\,\mathrm{km\,s^{-1}}$	$100\,\mathrm{km\,s^{-1}}$
	τ	Uniform	0.033	0.075
SARAS	σ	Log-Uniform	0.01 K	1 K
	a_0	Uniform	3.54	3.55
	a_1	Uniform	-0.23	-0.21
	a_2	Uniform	0	0.01
	a_3	Uniform	-0.01	0
	a_4	Uniform	0	0.01
	a_5	Uniform	-0.01	0.01
	a_6	Uniform	-0.01	0.01

et al. 2022). Note, that we treat α, E_min and t_delay as continuous parameters like Bevins et al. (2022b) rather than discrete parameters or fixing their values as was done in previous works (Bevins et al. 2022c; HERA Collaboration et al. 2023; Pochinda et al. 2023), allowing the emulator to interpolate between the discrete values provided by the simulation data set.

With all terms in equation (15) fully specified, we can now present the constraints we find from individual experiments and our joint analysis.

5 RESULTS

In this section, we present the parameter constraints from individual experiments, before advancing to our joint constraints. We then discuss our marginalized posterior on A_r and the interpretation thereof. Finally, we will consider our A_r constraints in the context of a superconducting cosmic string model.

The tightest constraints we see in our analysis are on combinations of the parameters A_r, $f_{*,\mathrm{II}}$, $f_{*,\mathrm{III}}$, and f_X. This is similar to what was found in previous studies (Abdurashidova et al. 2022a; Bevins et al. 2022b) that investigated models with synchrotron excess radio backgrounds, though those studies had a single star formation efficiency parameter. We depict these constraints for the individual experiments in Fig. 2. Such a result was expected due to these parameters having the greatest impact on the 21-cm signal and X-ray background. Higher A_r enhances the 21-cm signal magnitude as was seen in Fig. 1, while strong X-ray heating caused by high values of $f_{*,\mathrm{II}}f_\mathrm{X}$, or $f_{*,\mathrm{III}}f_\mathrm{X}$ typically suppresses the magnitude of the 21-cm signal. Furthermore, the interplay of $f_{*,\mathrm{II}}$, $f_{*,\mathrm{III}}$, and f_X determines both the magnitude of the X-ray background and the timing and strength of key features in the 21-cm signal, for example, the power spectrum heating peak.

Considering each experiment in turn, we find the HERA upper limits act to rule out a corner of models in $A_\mathrm{r} - f_\mathrm{X}$ space with high A_r values $\gtrsim 0.01$ and low f_X values $\lesssim 1$. This region corresponds to strong radio backgrounds and weak heating, hence large 21-cm power spectra values, thus leading to this region being excluded by the HERA 21-cm power spectrum limits. In addition, HERA disfavours but does not rule out, the combination of either low $f_{*,\mathrm{II}}$ and low f_X, or

low $f_{*,\mathrm{III}}$ and low f_X, since these also correspond to weaker heating. The combinations of either high E_min and high A_r, or low f_X and high V_c, are also seen to be disfavoured, discussed further in Appendix A and are similarly attributable to weak X-ray heating, strong radio backgrounds, or both. From the marginalized A_r posterior, we find HERA disfavours A_r values above 0.03 at 68 per cent confidence.

The SARAS 3 results are less constraining, with the principle constraint from SARAS 3 being a ruling out of a small region of high $A_\mathrm{r} \gtrsim 0.1$ and high $f_{*,\mathrm{III}} \gtrsim 0.15$ parameter space. This region corresponds to vigorous early star formation with strong radio backgrounds. SARAS 3 rules out such models as they predict a deep absorption trough minimum within its redshift range of 15.7–24.8. The lack of constraints from SARAS 3 on the $A_\mathrm{r} - f_\mathrm{X}$ parameter space is somewhat surprising given the constraints Bevins et al. (2022b) found on a similar synchrotron excess radio background model using the same data. We find the principal difference between the two models that leads to the weaker constraining power of the SARAS 3 measurements is the change of radio background exponents, $B_\mathrm{r} = 2.6$ in their study, to $B_\mathrm{r} = 2.25$ in ours. The weaker evolution of the excess radio background in our study leads to smoother and later 21-cm global signal minima. As a result, many high A_r low f_X models are not ruled out as might be expected due to the global signal absorption minimum moving outside the SARAS 3 band (as was shown in Fig. 1), making the global signal smooth across the SARAS 3 band and thus indistinguishable from the galactic foregrounds. Consequently, in these cases, the deep 21-cm signal can also be fit by the foreground model, leading to a degeneracy between foreground parameters and 21-cm signal parameters. This is confirmed via our finding of correlations in our 2D posteriors between A_r and the foreground parameters a_0, a_1, and a_2, shown in Fig. 3, whereas Bevins et al. (2022b) found their astrophysical and foreground parameter spaces to be independent. Due to this degeneracy, both the astrophysical parameter and foreground parameter constraints we find from SARAS 3 are weakened.

As is anticipated, the constraints from the X-ray background measurements are principally on the X-ray emission efficiency of (both Pop II and Pop III) star-forming haloes f_X, with the highest f_X values >100 almost entirely ruled out. The $f_{*,\mathrm{II}} - f_\mathrm{X}$ joint distribution shows the multiplicative degeneracy between these two parameters, with lower $f_{*,\mathrm{II}}$ values ruled out as f_X is increased. A weaker version of this trend is seen in the $f_{*,\mathrm{III}} - f_\mathrm{X}$ joint posterior. As there are far fewer total Pop III stars than Pop II stars, the X-ray background rules out a smaller region in $f_{*,\mathrm{III}} - f_\mathrm{X}$ than $f_{*,\mathrm{II}} - f_\mathrm{X}$ space.

We thus find that each of the individual observables rules out different regions of parameter space. This is reflected in our joint analysis results, where the complementarity of these experiments is made clear by a larger region of the total parameter space being ruled out or disfavoured when compared to any of the experiments individually. To quantify this statement more concretely, in our joint analysis, 51 per cent of the astrophysical prior is ruled out, whereas HERA, SARAS 3, and X-ray background measurements individually rule out 39 per cent, 6 per cent, and 5 per cent, respectively (see Appendix A3 for mathematical details). Most importantly, for this study, X-ray background measurements disfavouring high f_X when combined with the HERA constraints on $A_\mathrm{r} - f_\mathrm{X}$ rule out a portion of high A_r space that was allowed by HERA alone. Consequently, the disfavouring of high A_r above ~ 0.01 is enhanced through the joint analysis.

Since the focus of this study is on superconducting cosmic strings and thus A_r, from here on in, we concentrate on our A_r constraints and their implications rather than on the astrophysical parameters. For a detailed discussion on the insights that these data sets (and others)
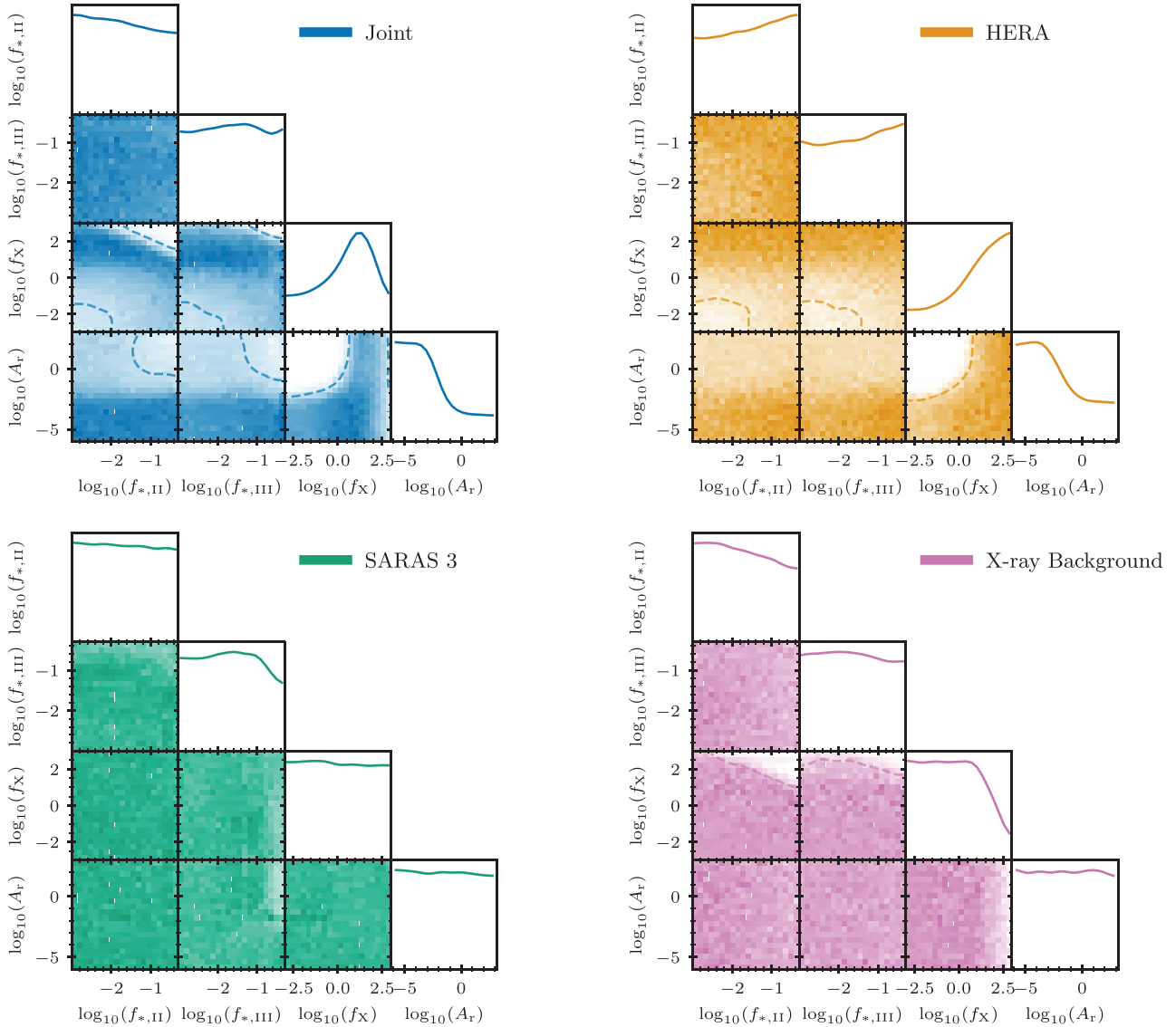
Figure 2. Constraints on key parameters from our joint analysis (top left, blue), HERA (top right, orange), SARAS 3 (bottom left, green), and the unresolved X-ray background (bottom right, pink). Shown are the 1D and 2D posteriors for the $f_{*,\mathrm{II}}$, $f_{*,\mathrm{III}}$, f_X, and A_r parameters. On selected 2D posteriors, 95 per cent confidence contours are shown as dashed lines to highlight disfavoured or ruled-out regions. Each of the three individual experiments rules out different regions of parameter space. HERA rules out a corner of low $f_\mathrm{X} \lesssim 1$ and high $A_\mathrm{r} \gtrsim 0.01$ values, SARAS 3 rules out the combination of high $f_{*,\mathrm{III}} \gtrsim 0.15$ and high $A_\mathrm{r} \gtrsim 0.1$, and the X-ray background strongly disfavouring high $f_\mathrm{X} \gtrsim 100$ values, in particular in conjunction with high $f_{*,\mathrm{II}}$. The joint analysis rules out a significantly larger portion of the total parameter space than any of the individual constraints showing their complementarity as probes of the early Universe. This and subsequent figure were produced using ANESTHETIC (Handley 2019).

provide on high redshift astrophysics, see Pochinda et al. (2023; Appendix A1, also provides a brief discussion on our astrophysical constraints). The marginalized posterior on $\log_{10}(A_\mathrm{r})$ from our joint analysis is shown in Fig. 4. Values of A_r below $\sim$0.001 are found to be fully consistent with all three considered data sets. Higher A_r values above this threshold become increasingly disfavoured, the posterior gradually decreasing, until it plateaus around $A_\mathrm{r} \sim 1.0$. We find these high $A_\mathrm{r} \gtrsim 1.0$ values to be less than a third as likely as the low $A_\mathrm{r} \lesssim 0.001$ values in light of the data. However, notably, our $\log_{10}(A_\mathrm{r})$ posterior is not close to zero in any region, and so no A_r values are confidently ruled out.

We hence can conclude that no strong constraints can be established on superconducting cosmic strings from current 21-cm signal

data, including from the latest HERA upper limits. This is in contrast to the findings of Brandenberger et al. (2019) who inferred constraints on the superconducting cosmic string parameters from the EDGES signal. The principle difference in our analysis is our inclusion of astrophysical uncertainties, in particular the unknown X-ray emission efficiency f_X of early Universe galaxies. As can be seen in Fig. 2, there remains a region of high f_X and high A_r values for which X-ray heating suppresses the 21-cm signal enhancement effect from the excess radio background, making these signals consistent with current 21-cm signal measurements. Thus, the presence of uncertain astrophysical heating prevents constraints on cosmic strings from HERA or SARAS 3 data.
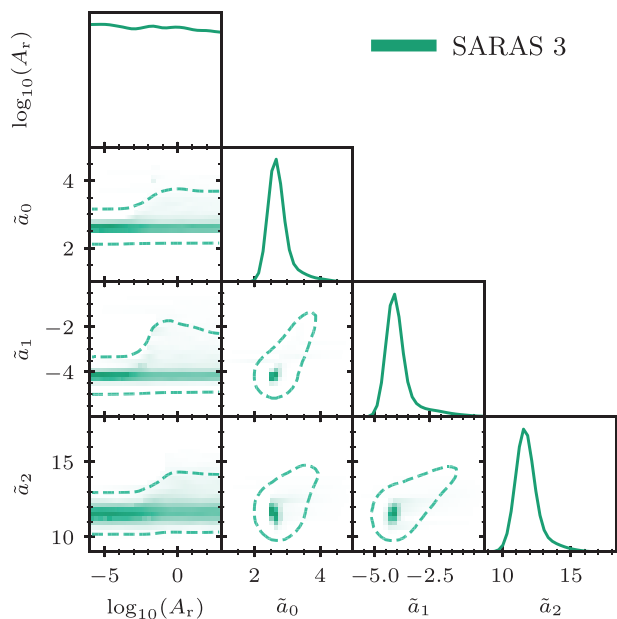
Figure 3. Posterior distribution of A_r and the first three SARAS foreground parameters from the SARAS 3 data analysis. For plotting clarity, the foreground parameters have been normalized via $\tilde{a}_0 = 10^4 a_0 - 35440$, $\tilde{a}_1 = 10^4 a_1 + 2190$, and $\tilde{a}_2 = 10^4 a_2$. As these transformations are linear, the priors over the transformed parameters remain uniform, and the correlations with other parameters remain unaffected. The 2D posteriors between A_r and the foreground parameters show correlations for A_r values in the range 0.001 to 10. These correlations are most evident in the top 95 per cent confidence contour (dashed line) in each panel, along which it can be seen that the foreground parameters increase to compensate for the deeper 21-cm signals that can be produced at high A_r values. As expected, since high A_r does not always produce deep 21-cm global signals, the lower 95 per cent confidence contours in these panels only show a weak change with A_r. The lack of correlations outside the above A_r range is due to the 21-cm signal not being significantly enhanced for A_r values below this range, and the impacts of high A_r saturating above this range as seen in Fig. 1 and discussed in Section 3.
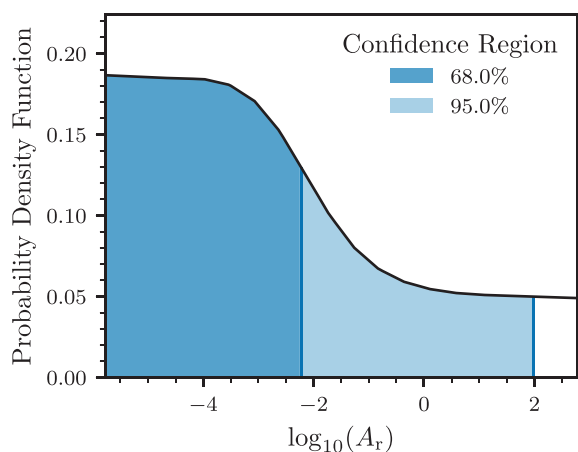
Figure 4. Joint analysis constraints on A_r, in the form of the posterior on $\log_{10}(A_r)$ (black line). High $A_r \gtrsim 1$ are seen to be disfavoured compared to low $A_r \lesssim 0.001$; however, the posterior never falls close to zero, and so no regions of A_r can be confidently ruled out. The 68 per cent and 95 per cent upper confidence regions are illustrated in dark blue and light blue, showing the favouring of A_r values <0.006 and <95, respectively. Since no values of A_r can be confidently ruled out, we conclude current 21-cm signal data are insufficient to rule out any superconducting cosmic string models.
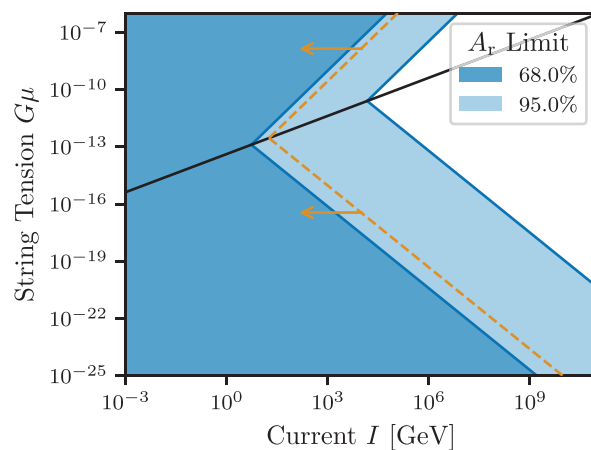
Figure 5. A_r confidence regions translated to superconducting cosmic strings parameter space. Here we assume $\beta = 10$, $\gamma = 10$, $\kappa = 1$, $\tilde{\kappa} = 1$, and $\chi = 10$ (Thériault et al. 2021). The dark (light) blue region has an A_r value less than the 68 per cent (95 per cent) upper confidence values from Fig. 4 of 0.006 (95). Also shown as an orange dashed line are the constraints from Brandenberger et al. (2019) assuming $\mathcal{R} = 1$, orange arrows indicate the direction of the permitted region. We see the 68 per cent confidence A_r contour corresponds roughly to the constraints previously found in Brandenberger et al. (2019). The 95 per cent confidence A_r contour shows even if we were to treat our disfavoured region of A_r as ruled out, which we do not advocate, the constraints on superconducting cosmic strings from current 21-cm signal data would be orders of magnitude weaker than have been previously stated.

There are, however, regions of A_r, and thus classes of superconducting cosmic strings, that are disfavoured by our analysis. We find upper confidence regions on A_r of <0.006 at the 68 per cent level and <95 at the 95 per cent level[11] also illustrated in Fig. 4. By assuming values for the dimensionless cosmic string model-specific parameters β, γ, κ, $\tilde{\kappa}$, and χ, we can translate these values to regions in the superconducting cosmic string parameters space of tension μ versus current I. Using the values from Thériault et al. (2021), $\beta = 10$, $\gamma = 10$, $\kappa = 1$, $\tilde{\kappa} = 1$, and $\chi = 10$, which were motivated by theoretical expectations and numeric simulations, we find the favoured and disfavoured regions illustrated in Fig. 5. Also shown on this figure in an orange-dashed line are the $\mathcal{R} = 1$ constraints from Brandenberger et al. (2019).

The region we find to be disfavoured based on our 68 per cent confidence value ($A_r > 0.006$) corresponds roughly to that Brandenberger et al. (2019) argued was excluded. Taken together, this would seem to be indicative that this is the level of constraints that could potentially be achieved from future 21-cm signal measurements. At the 95 per cent level, the disfavoured region corresponding to $A_r > 95$ is several orders of magnitude higher in string current than the previously estimated constraints. To reiterate, neither of these should be taken as constraints on superconducting cosmic strings as we do not convincingly rule out any of the A_r values we consider but are just given as a comparison to previous works and to facilitate speculation about the prospects for future constraints.

Due to the fact, we are already observing a disfavouring of high A_r values the prospects for constraints on superconducting cosmic

---

[11]Due to the ongoing debate about the existence of CMB heating (Venumadhav et al. 2018; Meiksin 2021), we performed a separate analysis with CMB heating disabled. The resulting conclusions did not change, and the confidence region values remained the same to within a few per cent.

strings from 21-cm signal observations soon seem promising. We found the HERA Phase 1 21-cm power spectrum upper limits (full 94 night season, HERA Collaboration et al. 2023) to be the most constraining part of our joint analysis and HERA is still in operation. So improved upper limits on the 21-cm power spectrum or even a detection are expected in the coming years from the later phases of their observations, which shall also cover lower frequencies (higher redshifts). In addition, proposed upcoming X-ray telescopes, such as *AXIS* (Mushotzky 2018), *ATHENA* (Nandra et al. 2013), or *LYNX* (The Lynx Team 2018), may be able to resolve further point sources, reducing the unresolved X-ray background and thus the upper limits on high redshift X-ray background. Finally, ongoing broader band 21-cm global signal experiments, such as REACH (de Lera Acedo et al. 2022) and MIST (Monsalve et al. 2023), should avoid the issues we encountered using the SARAS 3 data wherein the global signal minimum moves outside the band, and thus lead to more substantial constraints on A_r from 21-cm global signal null detections, or provide a definitive global signal detection.

6 DISCUSSION AND CONCLUSIONS

In this paper, we have performed a joint Bayesian analysis on the latest 21-cm signal data and measurements of the unresolved X-ray background in an attempt to constrain superconducting cosmic strings. Specifically, we consider, both individually and together, the constraints imposed by the SARAS 3 21-cm global signal experiment (Singh et al. 2022), the HERA Phase 1 21-cm power spectrum upper limits (HERA Collaboration et al. 2023), and combined X-ray background measurements from several satellites including *CHANDRA* (Hickox & Markevitch 2006; Harrison et al. 2016). We believe our analysis constitutes the first attempt to use the 21-cm power spectrum to constrain cosmic strings. Ultimately, we conclude that no such constraints can currently be inferred from the 21-cm signal, primarily due to the potential for heating by X-ray sources masking the impacts of the strings on the 21-cm signal.

We adopted the model of Brandenberger et al. (2019) for the excess radio background from superconducting cosmic strings, integrating it into the seminumerical 21-cm signal code 21CMSPACE. This allowed for the simulation of the 21-cm signal and X-ray background for different superconducting cosmic string parameters and astrophysical scenarios. Hence, facilitating constraints using the HERA, SARAS 3, and unresolved X-ray background measurements individually, and as a joint fit.

Due to the uncertainties surrounding the astrophysical parameters of the first galaxies, we followed a nested sampling-based Bayesian approach for our analysis. Such a method allowed us to rigorously marginalize the astrophysical and foreground parameters away as nuisance parameters. Since 21CMSPACE has a runtime of a few hours, we could not practically use it directly in our analyses. We instead trained neural network emulators on the outputs of 44 836 simulations and utilized these for our analysis, representing a $10^{3.5}$ times reduction in the number of simulations required than if we had directly called 21CMSPACE in our joint analysis, thus making our Bayesian approach feasible.

Analysis of the data sets individually revealed: the HERA 21-cm power spectrum upper limits rule out the combination of a strong radio background from cosmic strings and weak X-ray heating; the SARAS 3 21-cm global signal data eliminate a small area of strong radio backgrounds and efficient Pop III star formation; and X-ray background measurements rule out the highest rates of X-ray heating. By combining these data sets in our joint analysis, we found a disfavouring of a strong excess radio background, and hence

a region of high string current and high string tension parameter space. However, while this region was disfavoured at 68 per cent confidence, no part of the string parameter space was ruled out. We thus conclude the latest 21-cm cosmology data, at the moment of writing, gives no constraints on cosmic strings.

The difference between our conclusions and that of previous studies (e.g. Brandenberger et al. 2019) principally stem from our inclusion of the astrophysical uncertainties. Primary amongst these is the uncertainty in X-ray heating from high redshift sources, as efficient X-ray heating acts to suppress the 21-cm signal and thus mask any impacts of cosmic strings. If we knew for certain the X-ray emission efficiency of high redshift sources was $\lesssim 3 \times 10^{40}$ erg s yr^{-1} M$_\odot^{-1}$, then our analysis would predict similar cosmic string constraints to that of Brandenberger et al. (2019). However, theoretical expectations are that high redshift X-ray sources have efficiencies of 3×10^{40} erg s yr^{-1} M$_\odot^{-1}$ (Fragos et al. 2013) or greater (Sartorio et al. 2023; Liu et al. 2024), values for which we find no constraints on the strength of the radio background and hence no constraints on cosmic strings. This is of course all assuming the excess radio background is dominated by superconducting cosmic strings as we have done throughout this paper. The inclusion of other sources of excess radio background, such as high redshift radio galaxies (Reis et al. 2020), would weaken any constraints on cosmic strings and thus further strengthen our conclusions. We provide additional discussion on the astrophysical constraints from this work in Appendix A.

As we find some regions of cosmic string parameter space are already disfavoured, the prospects for near-future constraints on superconducting cosmic strings from 21-cm cosmology seem promising. Ongoing or upcoming experiments that could provide better limits or definitive detections of the 21-cm power spectrum include HERA (HERA Collaboration et al. 2023), NenuFAR (Mertens et al. 2021), LOFAR (Mertens et al. 2020), and SKA1-LOW (Koopmans et al. 2015), or for the 21-cm global signal, REACH (de Lera Acedo et al. 2022), PRIZM (Philip et al. 2019), MIST (Monsalve et al. 2023), SARAS 4, and EDGES 3. The broader bands of some of these upcoming global signal experiments should avoid the issue we encountered when attempting to extract cosmic string constraints from SARAS 3 data, that the global signal minima moved outside of the science band. In addition, the overdensity produced by cosmic string wakes may be able to be directly observed in SKA 21-cm signal images or detected in 21-cm three-point statistics (Brandenberger et al. 2010; Hernández & Brandenberger 2012; Hernández 2014; Maibach et al. 2021). Looking to the 2030s and beyond, there is also the potential for improved X-ray background measurements from proposed next-generation X-ray observatories, *AXIS* (Mushotzky 2018), *ATHENA* (Nandra et al. 2013), or *LYNX* (The Lynx Team 2018), which could be used in a future joint analysis. Any constraints from 21-cm cosmology on cosmic strings could then be used to supplement those from spectral distortions (Tashiro, Sabancilar & Vachaspati 2012), pulsar timing arrays (Quelquejay Leclere et al. 2023), big bang nucleosynthesis (Miyamoto & Nakayama 2013), reionization history, or the unexplained radio background (Cyr et al. 2023a, b) in a joint analysis, or provide an independent probe to confirm a discovery.

While this work was in its final stages of preparation, papers by Acharya et al. (2023) and Cyr et al. (2023b) were announced, proposing a new mechanism by which superconducting cosmic strings can impact the 21-cm signal, *soft photon heating*. These studies find that this heating from low frequency ($\lesssim 12$ MHz at $z = 20$) radio photons diminishes the magnitude of the 21-cm global signal absorption trough and thus prevents them from extracting any constraints on

cosmic strings when treating the claimed EDGES detection of the global 21-cm signal as a limit on the absorption trough depth. As we have found that astrophysical heating is already sufficient to prevent any meaningful constraints being placed on superconducting cosmic strings from current 21-cm signal data, including this additional heating would have strengthened our conclusions.

Should a definitive 21-cm signal detection be made, soft photon heating may prove advantageous for extracting constraints on superconducting cosmic strings. A cosmic string produced excess radio background on its own would be challenging to distinguish from cooling from interacting dark matter or a radio background from other sources. However, the combination of a radio background and soft photon heating, both from cosmic strings and hence with linked time evolutions, should break many degeneracies, allowing for firmer conclusions to be drawn. In addition, soft photon heating being effectively uniform is in stark contrast to astrophysical sources of heating, which are anticipated to be clustered around overdensities. The distribution of heating of the early Universe is inferable from the variation of the 21-cm power spectrum across wavenumber (Gessey-Jones et al. 2023), hence providing another signature to search for cosmic strings in the 21-cm signal. Thus while in this study we find no constraints on superconducting cosmic strings from 21-cm data, the outlook for doing so in the future appears optimistic.

DATA AVAILABILITY

The nested sampling inference products (e.g. chains) computed in this work are made available at https://zenodo.org/record/8362801 alongside code to reproduce most of the figures presented from said inference products. All other data and codes produced in this work are available on reasonable request to the corresponding author.

REFERENCES

Abadi M. et al., 2015, TensorFlow: Large-Scale Machine Learning on Heterogeneous Systems. Available at: https://www.tensorflow.org/
Abdurashidova Z. et al., 2022a, ApJ, 924, 51
Abdurashidova Z. et al., 2022b, ApJ, 925, 221
Acharya S. K., Cyr B., Chluba J., 2023, MNRAS, 523, 1908
Ajello M. et al., 2008, ApJ, 689, 666
Akins H. B. et al., 2023, ApJ, 956, 61
Albrecht A., Turok N., 1985, Phys. Rev. Lett., 54, 1868
Ashton G. et al., 2022, Nature Rev. Methods Primers, 2, 39
Barkana R., 2016, Phys. Rep., 645, 1
Barkana R., 2018, Nature, 555, 71
Barkana R., Fialkov A., Liu H., Outmezguine N. J., 2023, Phys. Rev. D, 108, 063503
Bevins H. T. J., Handley W. J., Fialkov A., de Lera Acedo E., Javid K., 2021, MNRAS, 508, 2923
Bevins H., Handley W., Lemos P., Sims P., de Lera Acedo E., Fialkov A., 2022a, preprint (arXiv:2207.11457)
Bevins H. T. J., Fialkov A., de Lera Acedo E., Handley W. J., Singh S., Subrahmanyan R., Barkana R., 2022b, Nature Astron., 6, 1473
Bevins H. T. J., de Lera Acedo E., Fialkov A., Handley W. J., Singh S., Subrahmanyan R., Barkana R., 2022c, MNRAS, 513, 4507
Bevins H., Handley W., Gessey-Jones T., 2023a, preprint (arXiv:2305.02930)
Bevins H. T. J., Handley W. J., Lemos P., Sims P. H., de Lera Acedo E., Fialkov A., Alsing J., 2023b, MNRAS, 526, 4613
Bevins H. T. J., Heimersheim S., Abril-Cabezas I., Fialkov A., de Lera Acedo E., Handley W., Singh S., Barkana R., 2024, MNRAS, 527, 813
Bowman J. D., Rogers A. E. E., Monsalve R. A., Mozdzen T. J., Mahesh N., 2018, Nature, 555, 67
Boylan-Kolchin M., 2023, Nature Astron., 7, 731
Brandenberger R. H., 1994, Int. J. Mod. Phys. A, 9, 2117
Brandenberger R. H., Danos R. J., Hernández O. F., Holder G. P., 2010, J. Cosmol. Astropart. Phys., 2010, 028
Brandenberger R., Cyr B., Shi R., 2019, J. Cosmol. Astropart. Phys., 2019, 009
Brandt W. N., Yang G., 2022, in Bambi C., Santangelo A. Handbook of X-ray and Gamma-ray Astrophysics. Edited by Cosimo Bambi and Andrea Santangelo. Singapore, p. 78
Cai Y.-F., Sabancilar E., Vachaspati T., 2012, Phys. Rev. D, 85, 023530
Churazov E. et al., 2007, A&A, 467, 529
Cohen A., Fialkov A., Barkana R., 2016, MNRAS, 459, L90
Cyr B., Chluba J., Acharya S. K., 2023a, preprint (arXiv:2308.03512)
Cyr B., Chluba J., Acharya S. K., 2023b, MNRAS, 525, 2632
de Lera Acedo E. et al., 2022, Nature Astron., 6, 984
D'Onofrio M., Rummukainen K., 2016, Phys. Rev. D, 93, 025003
Dowell J., Taylor G. B., 2018, ApJ, 858, L9
Eastwood M. W. et al., 2019, AJ, 158, 84
Ewall-Wice A. et al., 2016, MNRAS, 460, 4320
Ewall-Wice A., Chang T. C., Lazio J., Doré O., Seiffert M., Monsalve R. A., 2018, ApJ, 868, 63
Feng C., Holder G., 2018, ApJ, 858, L17
Fialkov A., Barkana R., 2019, MNRAS, 486, 1763
Fialkov A., Barkana R., Tseliakhovich D., Hirata C. M., 2012, MNRAS, 424, 1335
Fialkov A., Barkana R., Visbal E., Tseliakhovich D., Hirata C. M., 2013, MNRAS, 432, 2909
Fialkov A., Barkana R., Pinhas A., Visbal E., 2014a, MNRAS, 437, L36
Fialkov A., Barkana R., Visbal E., 2014b, Nature, 506, 197
Fialkov A., Cohen A., Barkana R., Silk J., 2017, MNRAS, 464, 3498
Field G. B., 1958, Proc. IRE, 46, 240
Fixsen D. J. et al., 2011, ApJ, 734, 5

Fragos T., Lehmer B. D., Naoz S., Zezas A., Basu-Zych A., 2013, ApJ, 776, L31

Fraser S. et al., 2018, Phys. Lett. B, 785, 159

Frontera F. et al., 2007, ApJ, 666, 86

Furlanetto S. R., Oh S. P., Briggs F. H., 2006, Phys. Rep., 433, 181

Gessey-Jones T. et al., 2022, MNRAS, 516, 841

Gessey-Jones T., Fialkov A., de Lera Acedo E., Handley W. J., Barkana R., 2023, MNRAS, 526, 4262

Grimm H. J., Gilfanov M., Sunyaev R., 2003, MNRAS, 339, 793

Gruber D. E., Matteson J. L., Peterson L. E., Jung G. V., 1999, ApJ, 520, 124

HERA Collaboration et al., 2023, ApJ, 945, 124

Handley W., 2018, J. Open Source Softw., 3, 849

Handley W., 2019, J. Open Source Softw., 4, 1414

Handley W. J., Hobson M. P., Lasenby A. N., 2015a, MNRAS, 450, L61

Handley W. J., Hobson M. P., Lasenby A. N., 2015b, MNRAS, 453, 4384

Harrison F. A. et al., 2016, ApJ, 831, 185

Hernández O. F., 2014, Phys. Rev. D, 90, 123504

Hernández O. F., Brandenberger R. H., 2012, J. Cosmol. Astropart. Phys., 2012, 032

Hickox R. C., Markevitch M., 2006, ApJ, 645, 95

Hills R., Kulkarni G., Meerburg P. D., Puchwein E., 2018, Nature, 564, E32

Hindmarsh M. B., Kibble T. W. B., 1995, Rep. Prog. Phys., 58, 477

Jones D., Palatnick S., Chen R., Beane A., Lidz A., 2021, ApJ, 913, 7

Kibble T. W. B., 1976, J. Phys. A Math. Gen., 9, 1387

Kibble T. W. B., 1980, Phys. Rep., 67, 183

Kibble T. W. B., 1982, Acta Phys. Polonica B, 13, 723

Klessen R. S., Glover S. C. O., 2023, ARA&A, 61, 65

Kolopanis M. et al., 2019, ApJ, 883, 133

Koopmans L. et al., 2015, in Advancing Astrophysics with the Square Kilometre Array (AASKA14). p. 1, preprint (arXiv:1505.07568)

Labbé I. et al., 2023, Nature, 616, 266

Leitherer C. et al., 1999, ApJS, 123, 3

Liu H., Outmezguine N. J., Redigolo D., Volansky T., 2019, Phys. Rev. D, 100, 123011

Liu B., Sartorio N. S., Izzard R. G., Fialkov A., 2024, MNRAS, 527, 5023

Mackay D. J. C., 2003, Information Theory, Inference and Learning Algorithms. Cambridge University Press, Cambridge

Madau P., Meiksin A., Rees M. J., 1997, ApJ, 475, 429

Magg M. et al., 2022, MNRAS, 514, 4433

Maibach D., Brandenberger R., Crichton D., Refregier A., 2021, Phys. Rev. D, 104, 123535

Marshall F. E., Boldt E. A., Holt S. S., Miller R. B., Mushotzky R. F., Rose L. A., Rothschild R. E., Serlemitsos P. J., 1980, ApJ, 235, 4

Mazumdar A., White G., 2019, Rep. Prog. Phys., 82, 076901

Mebane R. H., Mirocha J., Furlanetto S. R., 2018, MNRAS, 479, 4544

Mebane R. H., Mirocha J., Furlanetto S. R., 2020, MNRAS, 493, 1217

Medvedev P. et al., 2020, MNRAS, 497, 1842

Mertens F. G. et al., 2020, MNRAS, 493, 1662

Mertens F. G., Semelin B., Koopmans L. V. E., 2021, in Siebert A. et al., eds, SF2A-2021: Proceedings of the Annual meeting of the French Society of Astronomy and Astrophysics. p. 211, preprint (arXiv:2109.10055)

Mesinger A., 2019, The Cosmic 21-cm Revolution; Charting the first billion years of our universe. IOP Publishing, Bristol, UK

Mineo S., Gilfanov M., Sunyaev R., 2012, MNRAS, 419, 2095

Mirocha J., Mebane R. H., Furlanetto S. R., Singal K., Trinh D., 2018, MNRAS, 478, 5591

Miyamoto K., Nakayama K., 2013, J. Cosmol. Astropart. Phys., 2013, 012

Monsalve R. A. et al., 2023, preprint (arXiv:2309.02996)

Muñoz J. B., Dvorkin C., Loeb A., 2018, Phys. Rev. Lett., 121, 121301

Muñoz J. B., Qin Y., Mesinger A., Murray S. G., Greig B., Mason C., 2022, MNRAS, 511, 3657

Mushotzky R., 2018, in den Herder J.-W. A., Nikzad S., Nakazawa K., SPIE Bellingham, USAeds, Society of Photo-Optical Instrumentation Engineers (SPIE) Conference Series, Vol. 10699, Space Telescopes and

Instrumentation 2018: Ultraviolet to Gamma Ray. p. 1069929, preprint (arXiv:1807.02122)

Nandra K. et al., 2013, preprint (arXiv:1306.2307)

Pacucci F., Mesinger A., Mineo S., Ferrara A., 2014, MNRAS, 443, 678

Pedregosa F. et al., 2011, J. Machine Learn. Res., 12, 2825

Philip L. et al., 2019, J. Astron. Instrum., 08, 1950004

Planck Collaboration, 2020, A&A, 641, A6

Pochinda S. et al., 2023, preprint (arXiv:2312.08095)

Pritchard J. R., Furlanetto S. R., 2007, MNRAS, 376, 1680

Pritchard J. R., Loeb A., 2012, Rep. Prog. Phys., 75, 086901

Quelquejay Leclere H. et al., 2023, Phys. Rev. D, 108, 123527

Reis I., Fialkov A., Barkana R., 2020, MNRAS, 499, 5993

Reis I., Fialkov A., Barkana R., 2021, MNRAS, 506, 5479

Reis I., Barkana R., Fialkov A., 2022, MNRAS, 511, 5265

Sartorio N. S. et al., 2023, MNRAS, 521, 4039

Schauer A. T. P., Liu B., Bromm V., 2019, ApJ, 877, L5

Sikder S., Barkana R., Fialkov A., Reis I., 2024, MNRAS, 527, 10975

Sims P. H., Pober J. C., 2020, MNRAS, 492, 22

Singh S., Subrahmanyan R., 2019, ApJ, 880, 26

Singh S., Subrahmanyan R., Shankar N. U., Rao M. S., Girish B. S., Raghunathan A., Somashekar R., Srivani K. S., 2018, Exp. Astron., 45, 269

Singh S. et al., 2022, Nature Astron., 6, 607

Sivia D. S., Sivia D. S., Sivia D., 2006, Data analysis: a Bayesian tutorial., 2nd ed./d.s. sivia with j. skilling. edn. Oxford Science Publications, Oxford University Press, Oxford

Tanaka T., Hasegawa K., Yajima H., Kobayashi M. I. N., Sugiyama N., 2018, MNRAS, 480, 1925

Tashiro H., Sabancilar E., Vachaspati T., 2012, Phys. Rev. D, 85, 103522

The Lynx Team, 2018, preprint (arXiv:1809.09642)

Thériault R., Mirocha J. T., Brandenberger R., 2021, J. Cosmol. Astropart. Phys., 2021, 046

Vachaspati T., Vilenkin A., 1985, Phys. Rev. D, 31, 3052

Vanchurin V., Olum K. D., Vilenkin A., 2006, Phys. Rev. D, 74, 063527

Venumadhav T., Dai L., Kaurov A., Zaldarriaga M., 2018, Phys. Rev. D, 98, 103513

Verner D. A., Ferland G. J., Korista K. T., Yakovlev D. G., 1996, ApJ, 465, 487

Vilenkin A., 1981, Phys. Rev. Lett., 46, 1169

Visbal E., Barkana R., Fialkov A., Tseliakhovich D., Hirata C. M., 2012, Nature, 487, 70

Witten E., 1985, Nucl. Phys. B, 249, 557

Wouthuysen S. A., 1952, AJ, 57, 31

Yajima H., Khochfar S., 2015, MNRAS, 448, 654

APPENDIX A: ASTROPHYSICAL CONSTRAINTS

While the concentration of this study was on superconducting cosmic strings, our nested sampling-based methodology also produces astrophysical constraints as a by-product. These were briefly discussed in Section 5. Here, we go into more detail about the constraints on each astrophysical parameter (Section A1). In addition, we present the functional posteriors on each of the observables employed (Section A2) and quantify which data set is the most constraining in our analysis (Section A3).

A1 Astrophysical parameter constraints

The constraints on all astrophysical parameters and A_r from our joint analysis are shown in Fig. A1. For ease of comparison on the 1D posteriors, we also depict the constraints from HERA, SARAS 3, and the X-ray background individually. Considering the 1D posterior and 2D posteriors of each astrophysical parameter, we find:
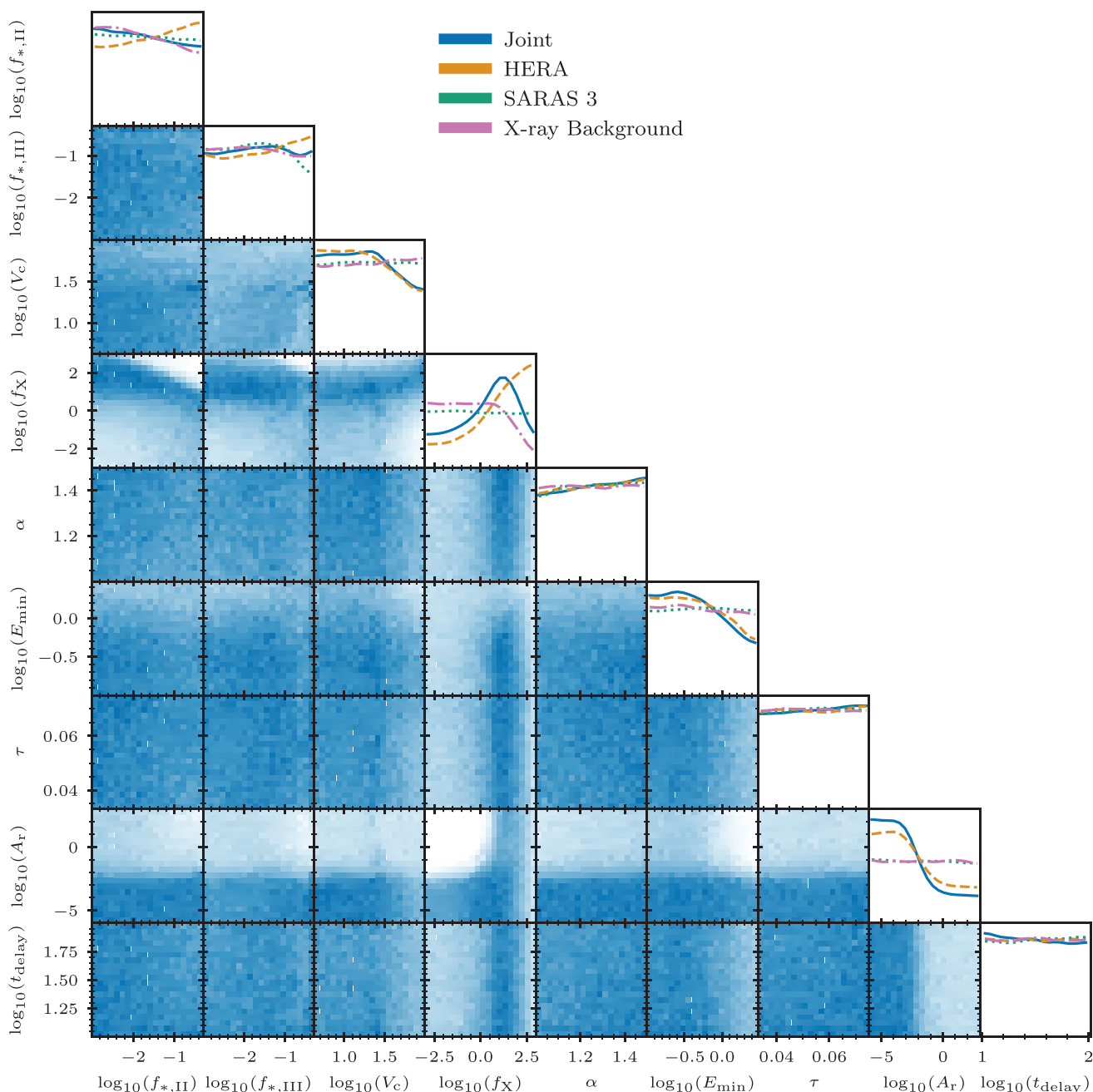
Figure A1. Constraints from our joint analysis on the astrophysical parameters and A_r. A subset of this corner plot was depicted in Fig. 2. The 2D posteriors depict only the constraints from the joint analysis, whereas the 1D posteriors show the joint analysis (blue solid) alongside the results from HERA (orange dashed), SARAS 3 (green dotted), and the X-ray background (pink dot–dashed). In the 1D posteriors, moderate constraints are seen on f_X and A_r, with weaker constraints on $f_{*,\text{II}}$, V_c and E_{min}. No constraints are seen on τ, α or t_{delay}. We find that the combination of $E_{\text{min}} \gtrsim 1.0\,\text{keV}$ and $A_r \gtrsim 0.1$ is ruled out due to high E_{min}, leading to inefficient X-ray heating and thus strong 21-cm signals. Since both f_X and E_{min} impact the efficiency of X-ray, heating a degeneracy between them is apparent in the disfavoured region of their joint posterior. Similarly, due to the combination leading to weak X-ray heating, we also observe the combination of $V_c \gtrsim 30$ and $f_X \lesssim 1$ to be disfavoured.

(i) $f_{*,\text{II}}$: A slight disfavouring of high $f_{*,\text{II}}$ is seen, principally driven by the X-ray background constraints. The multiplicative degeneracy between $f_{*,\text{II}}$ and f_X is evident in their joint posterior, with $f_{*,\text{II}}f_X \gtrsim 5$ ruled out by the X-ray background, and $f_{*,\text{II}}f_X \lesssim 0.001$ disfavoured by HERA.

(ii) $f_{*,\text{III}}$: The 1D posterior of $f_{*,\text{III}}$ shows no clear disfavoured values due to the competing influences of the three observables largely cancelling. SARAS 3 can rule out deep early global signal

minima, leading to the disfavouring of the combination of $f_{*,\text{III}} \gtrsim 0.15$ and $A_r \gtrsim 0.1$. The X-ray background rules out $f_{*,\text{III}}f_X \gtrsim 50$, while HERA disfavours the strong heating from $f_{*,\text{III}}f_X \lesssim 0.001$.

(iii) V_c: Values of $V_c > 30$ are found to be slightly disfavoured due to HERA. The joint posteriors reveal this is driven by HERA disfavouring the combination of $V_c \gtrsim 30$ and $f_X \lesssim 1$. Since high V_c values lead to lower star formation rates, this region would correspond to weak X-ray heating, which we have previously seen

HERA rules out in combination with strong radio backgrounds, thus explaining these trends.

(iv) f_X: Both HERA and the X-ray background provide constraints on f_X. This can be seen clearly in the 1D posterior where HERA disfavours $f_X \lesssim 1$ while the X-ray background disfavours $f_X \gtrsim 100$, leading to the joint constraint moderately favouring $f_X \sim 10$. The joint posterior of f_X and A_r is the strongest constrained of the 2D joint posteriors in the astrophysical part of the parameter space, with a ruling out of $f_X \lesssim 1$ and $A_r \gtrsim 0.01$. In addition to the previously discussed constraints, we see a disfavouring of a region of the $E_{min} - f_X$ joint distribution where $f_X \sim 10$ and $E_{min} \gtrsim 1.5\,\mathrm{keV}$. This constraint originates from HERA ruling out high radio backgrounds and weak X-ray heating. Higher E_{min} leads to a harder X-ray spectrum and, since higher energy X-rays have a lower cross-section in the IGM, weaker X-ray heating. This also explains the apparent degeneracy between f_X and E_{min} on the low f_X boundary of this disfavoured region as both high f_X and low E_{min} lead to increased X-ray heating.

(v) α: No constraints are seen on α.

(vi) E_{min}: Due to HERA disfavouring weak X-ray heating and strong radio backgrounds, we see a disfavouring of high E_{min} values, and the ruling out of the combination of $A_r \gtrsim 0.1$ and $E_{min} \gtrsim 1.0\,\mathrm{keV}$. For reference, early Universe X-ray binary spectra are predicted to have an E_{min} in the range 0.1–1.0 keV (Fragos et al. [2013]; Sartorio et al. [2023]).

(vii) τ: No constraints are seen on τ. This is consistent with previous studies that constrained early Universe astrophysics with HERA Phase 1 upper limits (e.g. Abdurashidova et al. [2022a]; HERA Collaboration et al. [2023]; Bevins et al. [2024]).

(viii) t_{delay}: No constraints are seen on t_{delay}.

Pochinda et al. ([2023]) previously found constraints on $f_{*, \mathrm{II}}, f_{*, \mathrm{III}}$, f_X, and V_c from the same data sets considered here; however, no constraints on E_{min} were reported in that study. Our discovery of constraints on E_{min} suggests future analyses may want to adopt the methodology utilized here, and in Bevins et al. ([2022b]), of allowing neural network emulators to interpolate between discrete values and then sampling over the parameter continuously to gain additional insights into the astrophysics of the early Universe.

A2 Functional posteriors of observables

An alternative perspective on our constraints is to view the functional posteriors of the observables themselves[12] rather than the parameter posteriors. These allow us to verify that our posteriors are consistent with observations, as well as determine which data sets are the most constraining, and reveal where the most uncertainty remains in these observables, potentially informing future observations.

The functional posterior of the 21-cm power spectrum at $k = 0.34\,h\,\mathrm{cMpc}^{-1}$ ($0.23\,\mathrm{cMpc}^{-1}$) is depicted in Fig. A2 for each of our four analyses. As was expected, we find the HERA data to be the most constraining on the 21-cm power spectrum and thus to dominate the joint constraints. SARAS 3 rules out strong 21-cm power spectra at redshifts $z > 15$ since these would be accompanied by a deep global signal in the SARAS 3 band. The X-ray background provides no constraint on the power spectrum. Overall, in the joint constraint, we find a large contraction of the allowed 21-cm power spectrum space from the prior to posterior showing the statistical power of the existing HERA upper limits. A comparison of the posterior

and prior also reveals the greatest uncertainty remains in the 21-cm power spectrum at high redshifts, motivating 21-cm power spectrum observations targeting $z > 15$ such as those underway by NenuFAR (Mertens et al. [2021]) and OVRO-LWA (Eastwood et al. [2019]).

In Fig. A3, we show the equivalent 21-cm global signal functional posteriors. Again, the X-ray background provides minimal constraints. The constraints from SARAS 3 are weak, ruling out only the deepest 21-cm signals at redshift 12–24, with no contraction between prior and posterior for $z < 12$. HERA provides the strongest 21-cm global signal prior to posterior contraction, ruling out the deepest global signals up to $z \sim 20$, and strongly constraining the global signal below the HERA observation band ($z < 11.1$). The $z < 20$ constraints from HERA and $z > 12$ constraints from SARAS 3 lead to a large contraction between the prior and posterior in the joint analysis. The deepest permitted global signals from said joint analysis have their minimum between $z = 14$ and 18, suggesting future global signal experiments should aim to cover this redshift range.

Finally, we find HERA and SARAS 3 have no significant constraining power on the X-ray background, with their functional posteriors nearly identical to the prior. As a result, the joint analysis constraints are entirely dominated by the X-ray background measurements, see Fig. A4.

A3 Quantifying constraining power

Previously, we have found qualitatively that of the data sets we consider, the HERA power spectrum upper limits provide the strongest constraints on high redshift astrophysics and A_r. However, a joint analysis still leads to a substantial improvement in constraining power over individual experiment constraints. Here, we quantify these statements more concretely.

In the case of a top-hat prior and posterior, there is an intuitive geometric measure of the constraining power of a data set, the percentage of the parameter space volume that is consistent with the data ($\%_{cons}$; i.e. the parameter space volume of the posterior over the parameter space volume of the prior). Using $\%_{cons}$, the constraining power of data sets can then be compared, with lower percentages indicating greater constraining power.

Unfortunately, if the posterior (or prior) is not a top-hat distribution, its parameter space volume is no longer well defined as there is no unambiguous inside and outside of the distribution in parameter space. Consequently, the above definition of $\%_{cons}$ breaks down. However, the notion of the percentage of the prior that is consistent with the data can still be defined using information theory. The amount of information gained through an experiment or observation is given by the KL divergence $\mathcal{D}_{KL}$ between posterior and prior (Sivia, Sivia & Sivia [2006]). Additionally, one bit of information is the information gained from ruling out half of the prior possibilities (Mackay [2003]). Combining these results, we arrive at an information-theoretic definition of the percentage of the prior that is consistent with the data[13]

$$\%_{cons} \equiv 100 e^{-\mathcal{D}_{KL}}, \tag{A1}$$

which has previously been used for quantifying the constraining power of data sets in Bevins et al. ([2022b]). Since $\mathcal{D}_{KL} \geq 0$ with equality only when the prior and posterior are identical, this definition

---

[12]Computed and depicted using our emulators and FGIVENX (Handley [2018]).

[13]In this study, we use the $\log_e$ convention for $\mathcal{D}_{KL}$ and hence it is in units of nats rather than bits. If the $\log_2$ convention is used instead, the e in this equation should be replaced with 2.
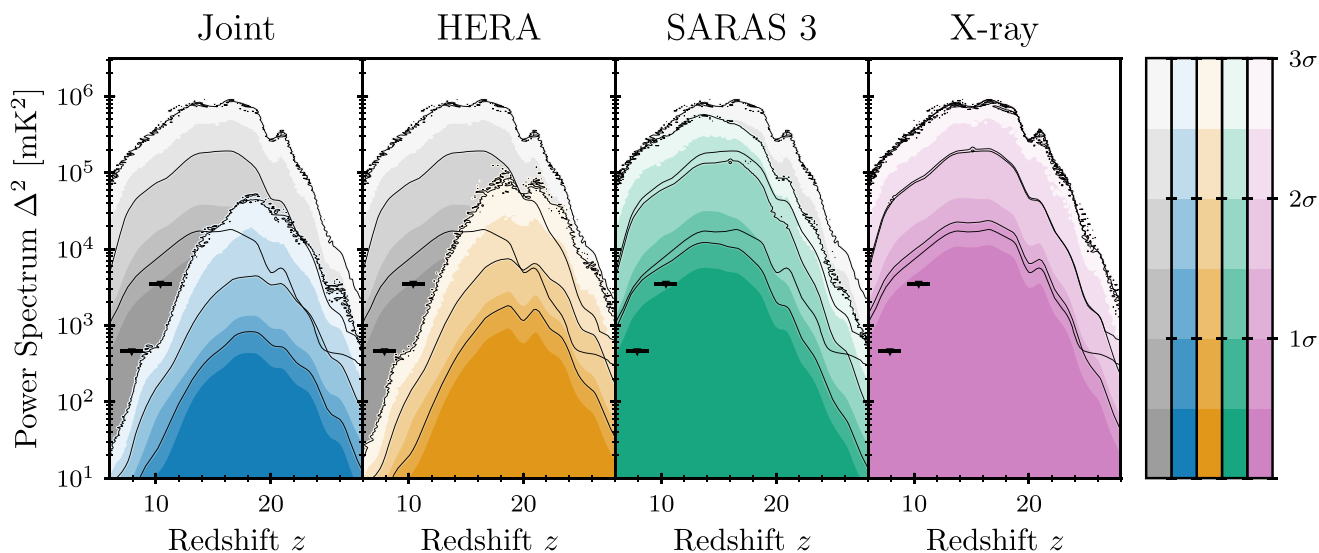
Figure A2. Functional posteriors on the 21-cm power spectrum at $k = 0.34 \, h \, \text{cMpc}^{-1}$ ($0.23 \, \text{cMpc}^{-1}$). The prior distribution is shown in grey, joint constraints posterior in blue, HERA posterior in orange, SARAS 3 posterior in green, and the X-ray background posterior in pink. No constraints on the 21-cm power spectrum are seen from the X-ray background, and the SARAS 3 constraints are weak, ruling out the strongest 21-cm power spectrum values at $z > 15$. The HERA data set constraints are strongest at lower redshifts <12, with little constraining power at $z > 22$. Despite the SARAS 3 and X-ray background constraints being weak, the joint analysis is not completely dominated by HERA, with the other two experiments improving the power spectrum constraints in the aforementioned high redshift region. The headline 21-cm power spectrum upper limits from HERA Collaboration et al. (2023) of $\Delta^2(k = 0.34 \, h \, \text{Mpc}^{-1}) \leq 457 \, \text{mK}^2$ at z = 7.9 and $\Delta^2(k = 0.36 \, h \, \text{Mpc}^{-1}) \leq 3496 \, \text{mK}^2$ at z = 10.4, are shown on the figure as black markers. The joint and HERA constraints posteriors are seen to be consistent with these limits, providing a sanity check for our methodology.
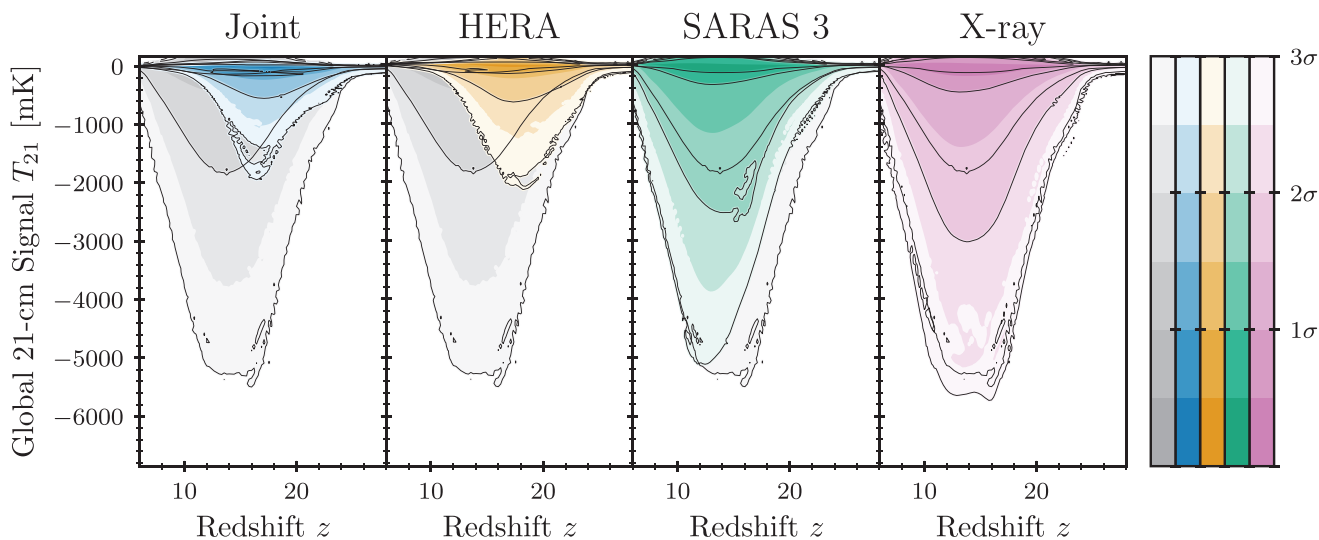

Figure A3. Functional posteriors on the 21-cm global signal. The prior distribution is shown in grey, joint constraints posterior in blue, HERA posterior in orange, SARAS 3 posterior in green, and the X-ray background posterior in pink. As was seen in Fig. A2 for the 21-cm power spectrum, no constraints are seen on the 21-cm global signal from the X-ray background. SARAS 3 provides moderate constraints on the 21-cm global signal, strongest in the SARAS 3 science band of redshift 15.7–24.8. The HERA power spectrum measurements are found to be quite constraining on the 21-cm global signal below $z = 20$ due to the link between the power spectrum magnitude and the global 21-cm signal. Our joint analysis shows a large contraction between posterior and prior, ruling out global signal amplitudes deeper than $-600 \, \text{mK}$ at 2σ and $-2000 \, \text{mK}$ at 3σ.

has the intuitive properties that it is always between 0 per cent and 100 per cent, with 100 per cent corresponding to the data having no constraining power. Furthermore, it can be shown that in the case of top-hat prior and posterior, it is equivalent to the parameter-space volume-based definition of %$_{\text{cons}}$ discussed previously. However, unlike the volume-based definition, the information-theoretic definition remains well-defined between any prior and posterior distribution (Mackay 2003). Thus, equation (A1) gives a versatile and well-
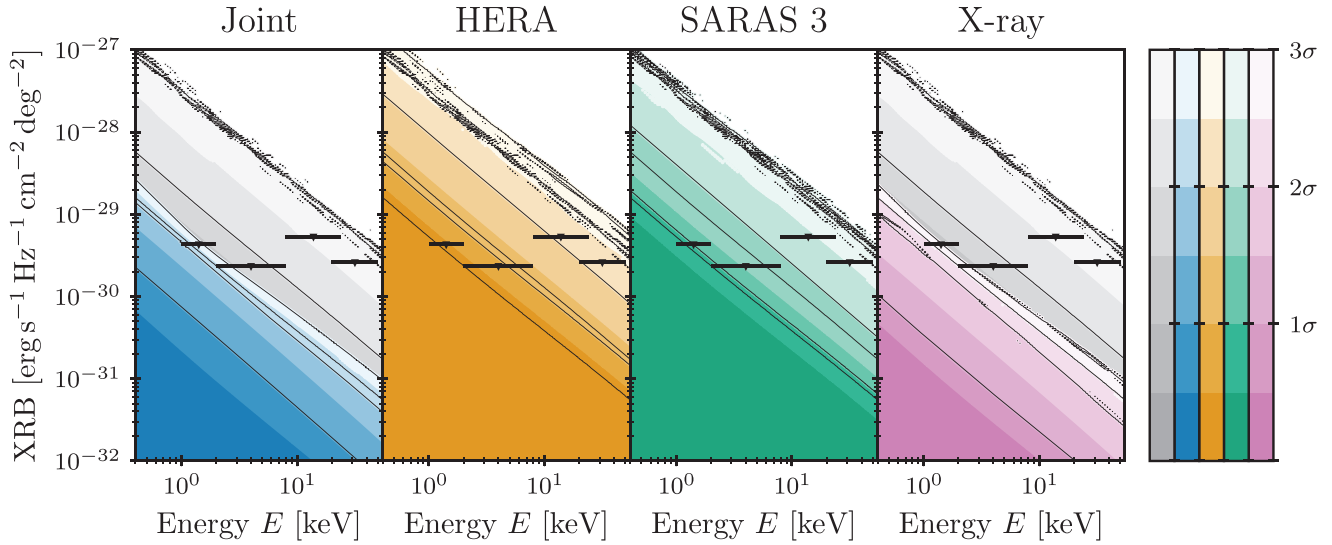
Figure A4. Functional posteriors on the X-ray background (XRB) from high redshift sources. The prior distribution is shown in grey, joint constraints posterior in blue, HERA posterior in orange, SARAS 3 posterior in green, and the X-ray background posterior in pink. X-ray background constraints are only seen to come from direct X-ray background measurements, with the HERA and SARAS 3 observations providing no constraints. The integrated unresolved X-ray background values listed in Table 1 are shown on the plot as black triangle markers, with the corresponding energy band indicated by a black bar. We find as expected that the X-ray background constraint and joint constraint posteriors are consistent with these upper limits, whereas the HERA and SARAS 3 posteriors are not.

motivated quantification to the constraining power of each of our data sets.

We are, however, not interested in the constraining power of the data sets on all the parameters, only the astrophysical and A_r parameters. To address this, in equation (A1), instead of the full $\mathcal{D}_{KL}$, we use the marginal KL divergence between the astrophysical prior and posterior, where nuisance (e.g. foreground) parameters have been integrated away (Bevins et al. 2024). Accordingly, we derive the percentage of the astrophysical prior consistent with the data and thus get a direct quantification of the constraining power of each data set on the parameters of interest. In practice, we calculate the marginal posteriors on the astrophysical and A_r parameters with MARGARINE (Bevins et al. 2022a; Bevins, Handley & Gessey-Jones 2023a; Bevins et al. 2023b).

The percentage of the astrophysical prior consistent with the data for each of the individual data sets is found to be 61 per cent for HERA, 94 per cent for SARAS 3 and 95 per cent for the X-ray background (see Fig. A5). Lastly, for the joint analysis, the corresponding value is 49 per cent. This confirms our earlier qualitative assessment that HERA is the most constraining individual data set, ruling out 39 per cent of the astrophysical prior whereas SARAS 3 and X-ray background are roughly equally constraining ruling out ∼ 5 per cent each. However, importantly, they rule out different regions of parameter space and so a joint analysis of the three provides stronger constraints, with 51 per cent of the prior ruled out, retroactively justifying our joint analysis methodology.

We can also perform a similar analysis using the marginal KL divergence on A_r alone, to determine the extent to which each analysis constrains our parameter of interest. For such an analysis, we find that in our joint fit, 87 per cent of the A_r prior is consistent with the data, with the equivalent values being 93 per cent for HERA,

and > 99 per cent for SARAS 3 and the X-ray background. This is consistent with what would be expected based on our $\log_{10}(A_r)$ 1D posteriors and further illustrates the benefits of performing a joint analysis on these data sets.
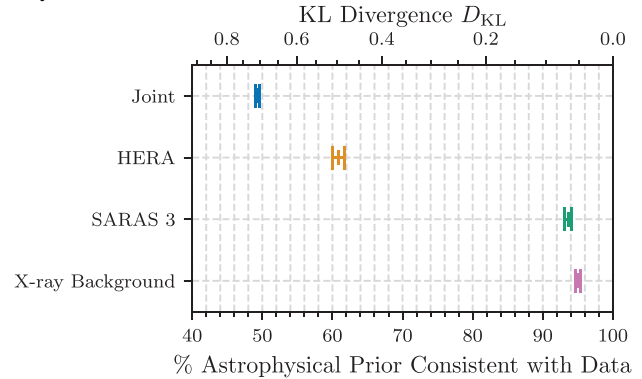

Figure A5. The percentage of the prior consistent with each data set and a joint analysis between them. The corresponding marginal KL divergence is given on the top axis. The percentages of prior consistent with the data are found to be 49 per cent for the joint analysis (blue), 61 per cent for HERA (orange), 94 per cent for SARAS 3 (green), and 95 per cent for the X-ray background (pink). We hence see that HERA is the most constraining individual data set, but is not dominant, with a significantly larger prior contraction in the joint analysis than when using any of the experiments individually.

This paper has been typeset from a T$_E$X/L^{A}T$_E$X file prepared by the author.